RMetS
Royal Meteorological Society

Regional comparison of West African convective characteristics: a TRMM-based climatology

Nick Guy* and Steven A. Rutledge
Department of Atmospheric Science, Colorado State University, Fort Collins, CO, USA

*Correspondence to: N. Guy, Colorado State University, Dept. of Atmospheric Sciences, 1371 Campus Delivery, Fort Collins, CO, USA. E-mail: guy@atmos.colostate.edu

A 13-year (1998–2010) climatology of mesoscale convective characteristics associated with the West African monsoon are investigated using precipitation radar and passive microwave data from the NASA Tropical Rainfall Measuring Mission satellite. Seven regions defined as continental northeast and northwest, southeast and southwest, coastal, and maritime north and south are compared to analyse zonal and meridional differences. Data are categorized according to identified African easterly wave (AEW) phase and when no wave is present. While some enhancements are observed in association with AEW regimes, regional differences were generally more apparent than wave vs. no-wave differences. Convective intensity metrics confirm that land-based systems exhibit stronger characteristics, such as higher storm top and maximum 30 dBZ heights and significant 85 GHz brightness temperature depressions. Continental systems also contain a lower fraction of points identified as stratiform. Results suggest that precipitation processes also varied depending upon region and AEW regime, with warm-rain processes more apparent over the ocean and the southwest continental region and ice-based microphysics more dominant over land, including mixed-phase processes. AEW regimes did show variability in stratiform fraction and ice and liquid water content, suggesting modulation of mesoscale characteristics possibly through feedback with the synoptic environment.

Key Words: West African monsoon; precipitation processes; African easterly waves; microphysics; TRMM climatology

Received 09 August 2011; Revised 17 November 2011; Accepted 22 November 2011; Published online in Wiley Online Library 15 December 2011

Citation: Guy N Rutledge S A. 2012. Regional comparison of West African convective characteristics: a TRMM-based climatology. *Q. J. R. Meteorol. Soc.* **138**: 1179–1195. DOI:10.1002/qj.1865

1. Introduction

The West African monsoon (WAM) is characterized by the northward migration of low-level (Gulf of Guinea) moisture to continental regions, and encompasses a complex interaction of multi-scale phenomena yet to be fully understood, in part due to limited long-term observations. The northward shift of the precipitation maximum supplies a majority of precipitation (Laurent *et al.*, 1998; Mathon *et al.*, 2002) to normally arid continental African regions, such as the Sahel, where mesoscale convective systems (MCSs) are responsible for the majority (> 80%) of rainfall totals (Le Barbé and Lebel, 1997; D'Amato and Lebel, 1998; Laurent *et al.*, 1998; Redelsperger *et al.*, 2002; Fink *et al.*, 2006).

The Saharan heat-low in northern Africa results in the convergence of dry northerly and moist southwesterly low-level flows, known as the intertropical discontinuity (ITD), which leads to strong baroclinicity across this boundary. These energetics along with the moist and dry convective contrasts lead to the development of the African easterly jet (AEJ), a strong, relatively dry mid-level jet with core centred around 600–700 hPa. Surface westerly winds are overlaid by the AEJ, with potentially unstable conditions

at low levels. This instability leads to the formation and maintenance of (often intense) MCSs (Aspliden *et al.*, 1976; Payne and McGarry, 1977; Houze and Betts, 1981; Barnes and Sieckman, 1984; Rowell and Milford, 1993; Hodges and Thorncroft, 1997; Mohr and Thorncroft, 2006; Nicholls and Mohr, 2010). These westward-moving systems generally exhibit a linear (squall line) morphology over the continent (Hamilton *et al.*, 1945; Eldridge, 1957; Bolton, 1984), a non–squall (amorphous) morphology over the eastern Atlantic (Schumacher and Houze, 2003, 2006; Fuentes *et al.*, 2008), and a transition stage upon exiting the coast (Sall and Sauvageot, 2005; DeLonge *et al.*, 2010).

Modulation of precipitation (and deep convective events) with synoptic disturbances in the form of African easterly waves (AEWs) has been suggested by many previous studies (Carlson, 1969; Burpee, 1974; Duvel, 1990; Diedhiou *et al.*, 1999; Fink and Reiner, 2003; Gu *et al.*, 2004; Petersen and Boccippio, 2004; Mekonnen *et al.*, 2006; Guy *et al.*, 2011). The wave disturbances, which may be initiated east of 20°E (Berry *et al.*, 2005; Thorncroft *et al.*, 2008), are maximized near the AEJ level and progress westward at ~ 8 m s^{-1}, with a wavelength of 2000–4000 km. Deep convection has been observed behind AEW troughs inland and in the eastern Atlantic and ahead of and within AEW troughs near the coast (Payne and McGarry, 1977; Reed *et al.*, 1977; Duvel, 1990; Machado *et al.*, 1993; Diedhiou *et al.*, 1999; Kiladis *et al.*, 2006). Westward-propagating MCSs in West Africa often move faster than AEW troughs (Aspliden *et al.*, 1976; Fortune, 1980; Fink *et al.*, 2006), and interact with the larger-scale environment through the transport of momentum (Moncrieff, 1992) and moisture (Lafore *et al.*, 1988) and can reinforce cyclonic rotation when embedded in an AEW trough (Barthe *et al.*, 2010).

A number of field campaigns have provided observational data for limited time periods, including the Global Atmospheric Research Program Atlantic Tropical Experiment (GATE: Houze and Betts, 1981) and the Convection Profonde Tropicale (COPT–81: Sommeria and Testud, 1984) experiment, providing important information regarding AEWs and MCS structure. More recently, the African Monsoon Multidisciplinary Analyses (AMM+A: Redelsperger *et al.*, 2006) campaign was organized to 'improve our knowledge and understanding of the West African monsoon'. The release of the International Science Plan for the second phase of AMMA (2010–2020; http://www.amma-international.org/IMG/pdf/ISP2_v2.pdf) summarized results from the first phase and stated the need to understand not only the meridional, but zonal characteristics of the WAM along the spectrum of phenomena that make up the WAM system. The characterization of regional convective characteristics encompasses mesoscale portions of the WAM and is useful in the validation of numerical simulations using explicit and parametrized formulations in cloud-resolving and general-circulation models.

Satellite-based studies of convective characteristics in various meteorological regimes have been used to look at the broad-scale aspects of convection and their coupling to large-scale forcing (Petersen and Rutledge, 2001; Toracinta *et al.*, 2002; Fink and Reiner, 2003; Nesbitt and Zipser, 2003; Petersen and Boccippio, 2004; Xu *et al.*, 2009; Leppert and Petersen, 2010). Additionally, regional characteristics have also been compared (Nesbitt *et al.*, 2000; Geerts and Dejene, 2005; Schumacher and Houze, 2006; Zipser *et al.*, 2006; Fuentes *et al.*, 2008; Liu *et al.*, 2008; Nicholls and Mohr, 2010). Within Africa, latitudinal (e.g. Geerts and Dejene, 2005) and longitudinal (e.g. Schumacher and Houze, 2006; Fuentes *et al.*, 2008) convective characteristics have been explored, though the regions in these studies generally encompassed at least one large horizontal domain, essentially smoothing out variability in one dimension. Ground-based radar has been used to study smaller mesoscale regions (Petersen *et al.*, 2003; Cifelli *et al.*, 2007; Guy *et al.*, 2011), though these studies encompassed short time periods and far smaller areas compared to satellite studies. Increased awareness of zonal and meridional inhomogeneity of precipitation and convective characteristics resulting from the AMMA project underscores the need for more detailed analysis of convective structures within a smaller regional domain, highlighting meso-α and -β scale systems.

Increasing attention has been paid to cloud properties (and microphysics) of West African convective systems (Cetrone and Houze, 2009, 2011; Bouniol *et al.*, 2010; Evaristo *et al.*, 2010; Penide *et al.*, 2010). Cloud properties, such as particle size and concentration, have been shown to vary by region (e.g. Protat *et al.*, 2010), and are important in model simulations due to factors such as radiation feedbacks and mass transport. Analysing these differences between distinct West African regions may provide useful information for model simulations.

This study reports on 'climatological' convective characteristics of precipitation features identified by the Tropical Rainfall Measurement Mission (TRMM) satellite in seven distinct regions, at a scale smaller than previous studies in an attempt to illuminate the inherent geographical differences that are present in West Africa. Characteristics were partitioned into AEW phase (trough, northerly, ridge and southerly) and when no AEW wave was present to examine differences associated with synoptic-scale regimes. This study intends to provide a climatological context in which to compare future regional model simulations of single MCSs and simulations of mesoscale and synoptic-scale domains where cloud-resolving model output may be compared. Additionally, relating results attained from ground-based radar observations to climatological spaceborne observations can help put differences in these observations into perspective.

2. Data and methodology

Seven regions, each encompassing a $6^\circ \times 6^\circ$ box, in West Africa were chosen (Figure 1) for analysis. The zonal distributions of northern (ConNE, ConNW, Cos, MarN) and southern (ConSE, ConSW, MarS) regions correspond to two commonly identified AEW latitude tracks (Reed *et al.*, 1977; Nitta *et al.*, 1985; Diedhiou *et al.*, 1999; Pytharoulis and Thorncroft, 1999; Thorncroft and Hodges, 2001; Fink and Reiner, 2003). The ConNE, Cos and MarN regions were contrasted for zonal variations and were chosen to correspond to ground-based radar locations used in Guy *et al.* (2011). Adjacent southern regions allowed the examination of meridional variability. Region size was chosen to restrict comparisons to meso-α size and smaller, while capturing a large enough sample size to produce a meaningful 'climatological' study. The ConNE region was centred north of the Niamey, Niger ground-based radar location used in Guy *et al.* (2011). This offset was necessary to ensure the ConSE region sampled mostly continental

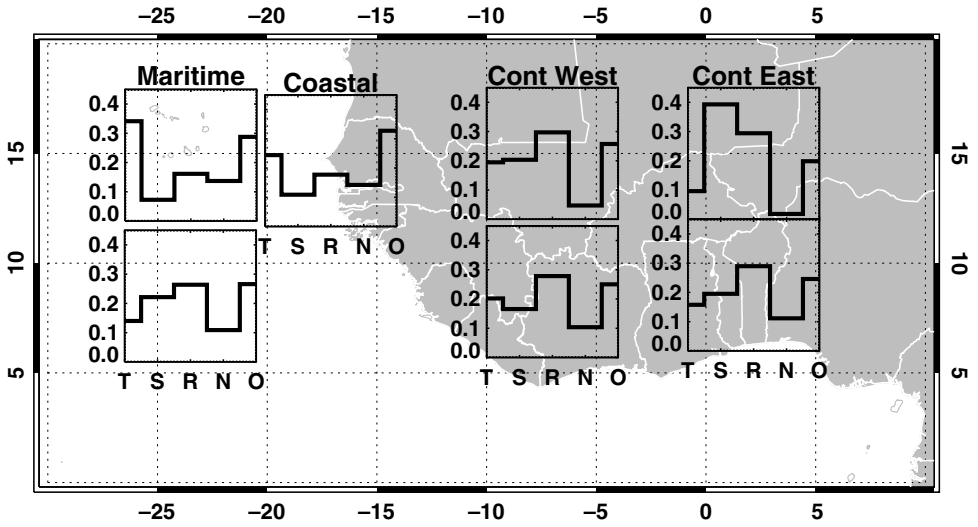

Figure 1. West African and Atlantic Ocean regions (6° × 6°) chosen for climatological analysis. Plots inside each regional domain indicate the relative proportion of precipitation features (using contiguous precipitation radar reflectivity) occurring in the trough ('T'), southerly ('S'), ridge ('R'), and northerly ('N') African easterly wave phases; and when no wave was identified ('O'). Fractions are calculated by using the number of features in each phase divided by the total number of features in that region.

convective systems and minimized extension into the Gulf of Guinea. The MarS region roughly encompassed the GATE domain corresponding to shipboard radar observations.

The primary sources of data in this study are TRMM precipitation radar (PR) and microwave imager (TMI) observations and retrievals (Kummerow *et al.*, 1998, 2000). The University of Utah TRMM precipitation feature (PF) database (Nesbitt *et al.*, 2000; Liu *et al.*, 2008) was employed to assess convective characteristics in each region from May to October (period of AEW activity) during 1998–2010. The PF database incorporates many standard product outputs (i.e. 2A25; TRMM PR 3-D reflectivity) along with calculated statistics (i.e. minimum 85 GHz microwave brightness temperatures); see Liu *et al.* (2008) and references therein for a complete discussion. Three-dimensional PR, 85 and 37 GHz polarization corrected temperatures (PCTs), and stratiform fraction were used in this study. Contiguous pixels of PR reflectivity with near-surface rain defined the PFs. Stratiform fraction was calculated for each PF by dividing the number of pixels identified as stratiform by the total number of pixels associated with the PF, which was also used in area calculations. The footprint of a PR pixel increased following the August 2001 TRMM satellite orbit boost to extend lifetime (approximately 18.5 km^2 pre-boost and 25.0 km^2 post-boost), which also increased the minimum detectable reflectivity threshold from 17 to 18 dBZ. Only PFs with area greater than 75 km^2 and at least one pixel of reflectivity greater than 30 dBZ were retained (Tables I–II).

Calculation of ice water mass and liquid water mass using three-dimensional PR data followed the methodology of Petersen *et al.* (2005). Briefly, vertical profiles (250 m spacing) of radar reflectivity (Z) for every PF were processed. Ice water content (IWC, from the −5°C level to echo top) was calculated for each vertical PR gate using an exponential size (mass, M) distribution in the form of an M–Z relationship (Carey and Rutledge, 2000):

$$IWC = 1000\pi\rho_i N_0^{3/7}\left(\frac{5.28\times10^{-18}}{720}Z\right)^{4/7}\ (\mathrm{g\,m^{-3}}), \quad (1)$$

Table I. Number of precipitation features identified using TRMM precipitation radar and associated with objectively analysed African easterly wave phase in northern regions in this study.

	Maritime North	Coastal	Continental Northwest	Continental Northeast
Trough	1372	1293	1021	443
Southerly	292	576	1066	1809
Ridge	649	940	1557	1354
Northerly	551	754	247	84
No AEW	1157	1735	1349	914
Total	4021	5298	5235	4607

Table II. Number of precipitation features identified using TRMM precipitation radar and associated with objectively analysed African easterly wave phase in southern regions in this study.

	Maritime South	Continental Southwest	Continental Southeast
Trough	3093	2896	1634
Southerly	4893	2377	2023
Ridge	5827	3992	3001
Northerly	2403	1487	1155
No AEW	5873	3587	2548
Total	22089	14339	10361

where IWC is mass per volume, Z is in mm^6 m^{-3}, N_0 is the constant intercept parameter (4×10^6 m^{-4}), and bulk ice density (ρ_i) varies between 100 and 800 g m^{-3} as a function of Z and precipitation type (stratiform or convective). Similarly liquid water content (LWC; from near surface to the 0°C level) was calculated for points over

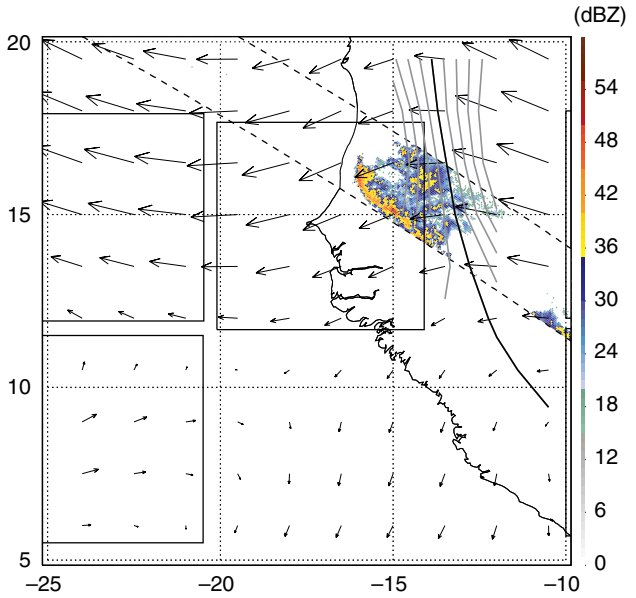

Figure 2. TRMM overpass 50098 at 0530 UTC 31 August 2006 showing precipitation radar reflectivity swath. Boxes are regions discussed in this study, with the swath passing through the coastal region. Arrows indicate 700 hPa wind vectors. The solid black line is the objectively identified African easterly wave trough axis for 0600 UTC on the same day. The grey contours show the identified trough region retained after thresholding procedure. Precipitation features within the coastal domain were identified as trough-associated for this case.

ocean (Tokay and Short, 1996) via:

$$LWC = 5.338 \times 10^{-4} Z^{0.813} (\mathrm{g\,m^{-3}}), \quad (2)$$

and for coastal and land points (Tokay *et al.*, 2002) via:

$$LWC = 3.5 \times 10^{-3} Z^{0.536} (\mathrm{g\,m^{-3}}). \quad (3)$$

The 0°C and −5°C levels were climatological heights (approximately 5 and 4 km, respectively) found as a function of location using National Centers for Environmental Prediction (NCEP) reanalysis data (Petersen *et al.*, 2005). Because of difficulties in calculating mass contents in mixed-phase conditions, no attempt was made to estimate IWC or LWC between the 0°C and −5°C levels. The IWC and LWC calculations are approximate as a number of assumptions are used to develop these relationships. Because this study will focus on comparing the relative trends and magnitude, any errors in relationships should not impact study results. It is also important to note that echo top corresponds to ∼ 17–18 dBZ (depending on pre- or post-boost), the minimum detectable signal for the PR, which obviously does not correspond to actual storm top height. Similar fractions of PFs occurred before the orbital boost in each region; therefore no bias was applied to any one region. LWC and IWC were vertically integrated to attain liquid water path (LWP) and ice water path (IWP) estimates and averaged for each PF. The bulk of IWC resides at reflectivity values above 17 dBZ, therefore the estimation of IWC should not be greatly impacted by the PR threshold.

All native and calculated data were partitioned according to AEW phase (trough, southerly, ridge and northerly) and no-wave regimes. The European Centre for Medium-range Weather Forecasts (ECMWF) interim reanalysis (ERA-Interim: Simmons *et al.*, 2007) zonal and meridional winds (fixed 1.5° gridded) were employed to diagnose AEW vorticity centres (via stream-function calculation, essentially eliminating non-divergent flow) at 700 hPa for West Africa (0–30°N, 30°E–30°W). Berry *et al.* (2007) developed a method to decompose the calculated stream-function vorticity into shear and curvature components, and to use the westward advection of curvature vorticity to identify AEW trough and ridge regions. In this methodology, trough or ridge axes were identified where westward advection of curvature vorticity is equal to zero. The same curvature vorticity threshold (0.5×10^{-5} s^{-1}) suggested in Berry *et al.* (2007) was used to distinguish between ridge and trough classifications (following manual inspection of multiple individual time steps, not shown). Removal of pseudo-troughs (-ridges) resultant from local minima (maxima) of non-divergent wind curvature was accomplished via a second thresholding mask. Points retaining trough or ridge classification following the masking procedures were identified as such. An example of a trough-classified system is shown in Figure 2.

Mean meridional winds at each longitude were calculated for each year to establish background flow. Criteria for southerly (northerly) phase designation followed the reasoning that negative (positive) curvature vorticity advection occurred east (west) of a trough, along with meridional wind components greater (less) than the calculated mean. Points that did not meet any of the criteria above were designated as being not associated with an AEW phase (no-wave). Bain *et al.* (2011) discussed limitations of the composite view of AEWs, noting that there is a spectrum of wave structures possible over West Africa. With this in mind, a specific distance from trough or ridge axes was not used as a classification criterion in this study. Instead, the algorithm employed can be used to identify regions consistent with dynamics of each wave phase. Analysis of these maps (not shown) revealed that the identified regions were slightly smaller than the 500 km distance associated with triggering and maintenance of convection (Berry, 2009; Nicholls and Mohr, 2010). Since regions are compared against one another, the large PF sample size should smooth out any natural variability of convective location within an AEW phase region; this should not impact the results of this study.

3. Results

3.1. *Precipitation feature characteristics*

Monthly frequency distributions for each region as a function of AEW phase (Figure 3) showed lower frequency of occurrence for PFs in northern regions compared to southern regions, where a more favourable thermodynamic environment (e.g. low-level moisture, vertical wind shear) exists during May–October. Nicholls and Mohr (2010) showed that intense convective systems, identified as the top 10th percentile of minimum 85 GHz PCTs, clustered near the baroclinic zone produced by the WAM system, while weaker systems showed no clustering (but were obviously more dense toward southern regions, see their Fig. 5). A seasonal peak in the drier northern regions was evident, consistent with the migration of the monsoon moisture and enhanced AEW activity. A greater number of PFs in northern continental regions associated with AEWs during May and June were related to the domain size which extended southward of the nominal location of

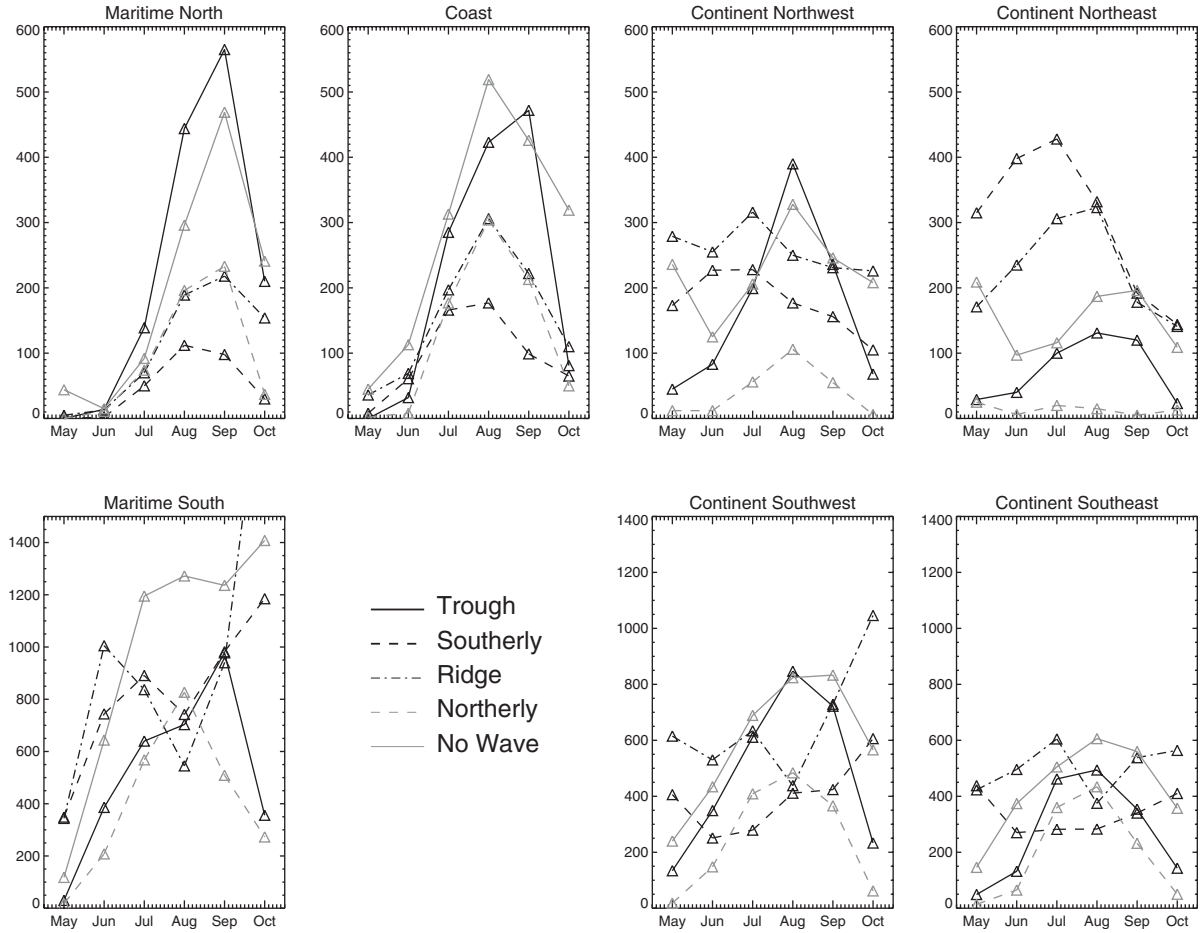

Figure 3. Precipitation feature frequency distribution in each study region during May–October. Each month is partitioned by objectively identified AEW trough (solid black), southerly (dashed black), ridge (dotted black), and northerly (dashed grey) phase, along with when no AEW phase (solid grey). Note the different ordinate axis scale between regions.

the intertropical convergence zone (ITCZ), capturing more consistent convective activity to the south during those months.

The highest AEW phase-associated PF frequencies (Figure 1) occur in the southerly phase in the ConNE region, trough phase in the coastal and MarN regions, and the ridge phase in ConNW, ConSW, ConSE and MarS regions. It is important to note that PFs represented snapshots of convective systems and genesis/lysis information may not be reliably extracted from these data alone. As mentioned previously, MCSs often travel faster than AEWs, and therefore life-cycle characteristics could be aliased to wave regimes other than the formative and decay stages. Despite this limitation, occurrence frequency results were consistent with previous studies (most of which concentrated on genesis/lysis of MCS with respect to AEW phase) that have found that deep convection occurs east of AEW troughs near the continental sites and west of and in the trough near the coast and Atlantic (Carlson, 1969; Payne and McGarry, 1977; Reed *et al.*, 1977; Diedhiou *et al.*, 1999; Fink *et al.*, 2006; Kiladis *et al.*, 2006; Laing *et al.*, 2008). Fink and Reiner (2003) and Laing *et al.* (2008), primarily using microwave and infrared observations for squall line and deep convective tracking, respectively, found a large fraction of systems were not associated with any AEW phase. Nearly equivalent or greater occurrence fraction was found in every region except ConNE (where the least PFs were observed in the no-wave phase).

Maximum storm height (MSH), corresponding to the highest detected pixel identified in raining columns (TRMM 2A23 product; rain characteristics), within a PF was used to compare vertical development between regions. Mean MSH over the continent was greater in the northern region (8.1–8.4 km vs. 7.3–7.5 km mean values for southern regions), while the maritime regions were the same (6.0 km). Mean values of MSH can obscure outliers (e.g. top 10 percentile) in the data; therefore it is of interest to examine the frequency distribution of observed heights. Cumulative frequency distributions (CFDs) of MSH for each region (Figure 4) indicated greater variability between AEW regimes over land, especially in ConSE. Frequency of PFs with MSH greater than 10 km increased from the Atlantic inland, with roughly 6–8% over the ocean, 10% at the coast, and 18–22% over land. Southern regions generally produced a higher frequency of taller convective systems (except ConNW), though mean values decreased due to the greater number of PFs with lower MSH values identified.

While the MSH is an indirect measure of the convective nature of systems, the majority of PFs in this study also contained multiple pixels identified as stratiform. Approximately 95% (90%) of PFs over land (ocean) had at least one pixel identified as stratiform. Not only does the stratiform component contribute to precipitation totals, but also plays an important role in the vertical heating profile of convective systems (Tao *et al.*, 1993, 2010), making it of keen interest to analyse stratiform fractions (Figure 5)

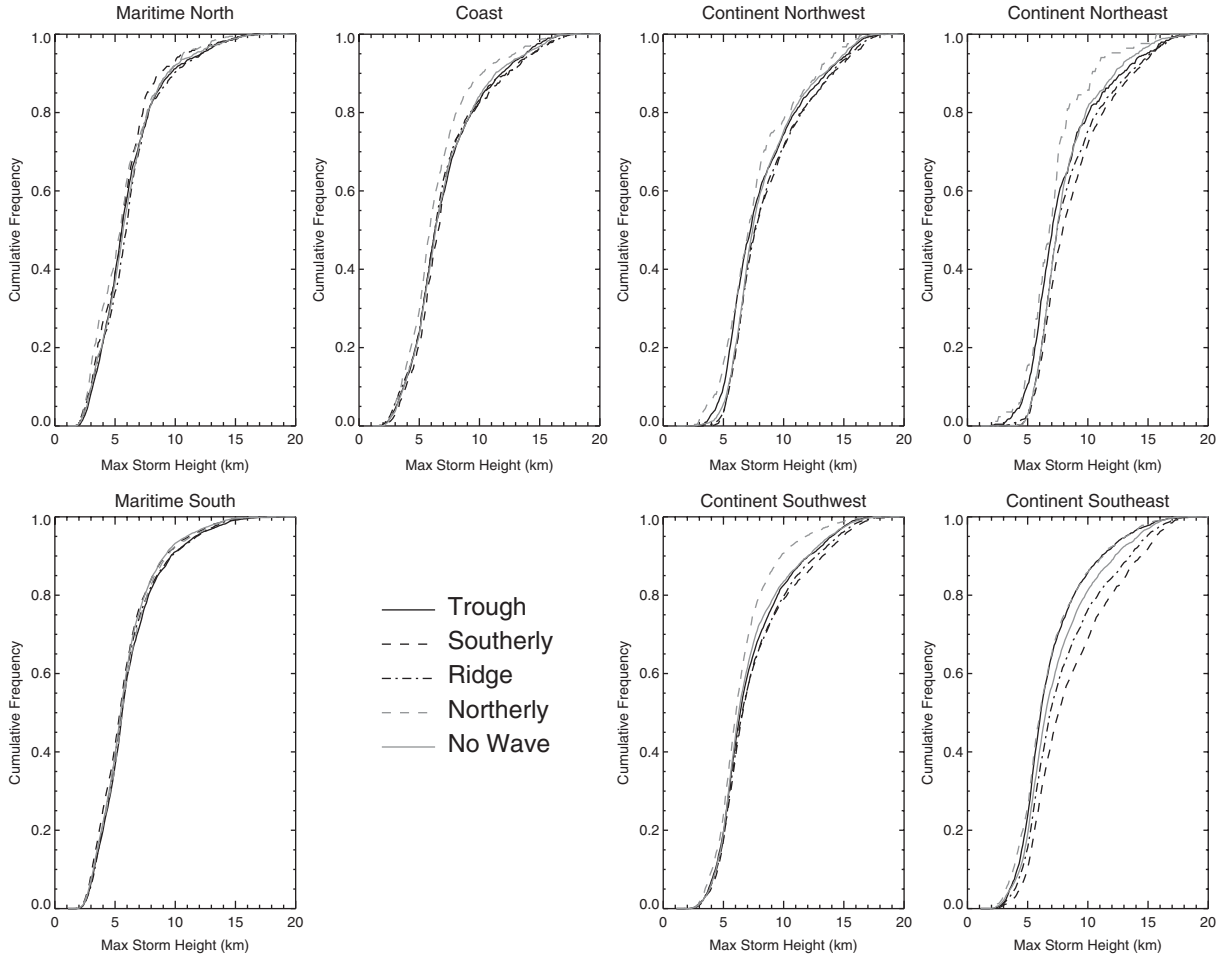

Figure 4. Cumulative frequency distributions of precipitation feature maximum storm height for each study region. Objectively identified AEW phases along with no identified AEW are displayed as in Figure 3.

for each region. Mean stratiform fractions were nearly the same (Table III) between regions, with a slight decrease eastward from the Atlantic and coastal regions ($\sim$ 67%) to continental regions ($\sim$ 61%). The shape of the CFD regional curves in Figure 5 showed that maritime regions experienced a higher occurrence of larger stratiform fraction. The separation of CFD curves for each AEW regime showed that large variability existed for stratiform fraction, as much as 20% in the case of ConSE. This result suggests different heating structures between AEW regimes, indicating the possibility of variable feedbacks onto both small- and large-scale atmospheric circulations.

As in Liu *et al.* (2008), mean PF area calculations showed larger systems over land than their oceanic counterparts (Table III). Over the continent, the northern regions produced larger mean PF area than southern regions, discernible in Figure 6 by the lower frequency of smaller events in ConNE and ConNW. In agreement with Guy *et al.* (2011), AEW regimes produced an increased occurrence of larger systems in the ConNE, ConNW and coastal regions. Environmental factors such as strong low-level vertical wind shear aid the organization of intense convective systems (Frank, 1978; Rowell and Milford, 1993; Johnson *et al.*, 2005; Mohr and Thorncroft, 2006; Nicholls and Mohr, 2010) over land. Stratiform precipitation is formed through the decay of convective regions and broad mesoscale ascent in the associated stratiform region (Zipser, 1969; Houze, 1977; Houze *et al.*, 1989). A global climatology of convective inhibition (CIN) using the ECMWF ERA-40 reanalysis product (Riemann-Campe *et al.*, 2009) showed higher mean CINs inland and in northern locations which may act as a cap, leading eventually to stronger convective development. Analysing the number of PFs in each overpass (not shown) showed a higher percentage of the occurrence of a single PF in the ConNE domain ($\sim$ 35%) compared to the other regions ($\sim$ 26%). Along with larger mean PF size (Table III), this supports the notion of suppression of small convective systems at the continental site.

Mean values of PF characteristics as a function of AEW regime are summarized in Figure 7 for each region. These results indicated changes in convective characteristics as a function of phase in each region. Trough and ridge AEW regimes exhibited similar characteristics in a mean sense. While the trough phase displayed a more widespread convective signature (higher stratiform fraction, larger area), ridge phase convection was slightly more intense (lower 85 GHz PCTs, higher MSH and 30 dBZ heights). The southerly phase generally indicated more isolated, intense convection (relatively lower stratiform fractions, higher MSH and 30 dBZ heights, higher 85 GHz PCTs); while a decrease in convective strength was observed at all sites during the northerly AEW phase (reduced MSH and 30 dBZ heights, lower 85 GHz PCTs, and larger stratiform fraction). Convection occurring when no AEW was identified was similar to that in the southerly AEW regimes, though an increased stratiform signature was evident. These differences

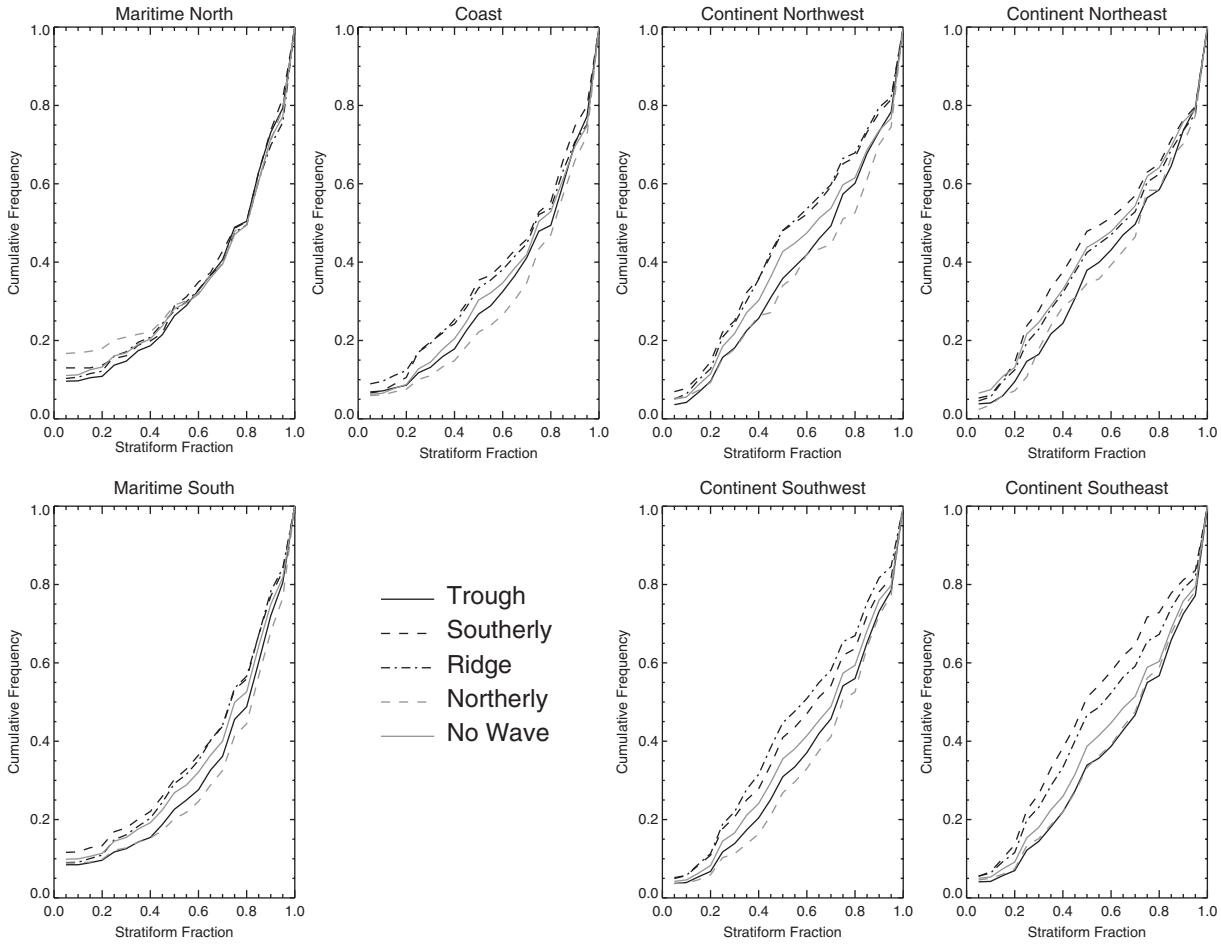

Figure 5. As in Figure 4, except for stratiform fraction.

Table III. Mean values of properties associated with precipitation features in the seven study regions during May–October, 1998–2010.

	Feature area (km^2)	Maximum storm height (km)	Maximum 30 dBZ echo height (km)	Minimum 85 GHz PCT (K)	Minimum 37 GHz PCT (K)	Stratiform fraction (%)
MarN	1004	6.0	3.8	260	279	66.5
MarS	1279	6.0	3.8	262	264	67.5
Coastal	1654	7.0	4.7	248	271	67.5
ConNW	1752	8.4	6.2	239	276	60.6
ConNE	1831	8.1	6.0	240	275	61.1
ConSW	1253	7.3	5.2	245	265	63.7
ConSE	1511	7.5	5.4	240	277	61.1

Regions: maritime north (MarN) and south (MarS), coastal, continental northwest (ConNW), northeast (ConNE), southwest (ConSW) and southeast (ConSE).

suggested that analysis of vertical convective characteristics, along with associated precipitation processes, may result in differences between AEW regime and region.

3.2. *Vertical structure*

Mean vertical profiles of convective (Figure 8) and stratiform (Figure 9) radar reflectivity were produced for each region and separated by AEW regime. Results above 17 km were noisy and contained a much smaller number of points as only the deepest convective systems reached those levels. Intra-region AEW regime profiles were similar in Figures 8–9, though convective profiles were stronger throughout in more eastward regions, that is, more interior to the continent. Coastal and continental convective profiles showed the largest deviations by AEW phase, where the southerly regime exhibited larger reflectivity values throughout the profile, which suggests stronger convective components associated with the southerly regime over land. Only the coastal location displayed a no-wave regime profile distinctive from AEW phases, in agreement with ground-based radar results in Guy *et al.* (2011), which examined the peak monsoon period (19 August–16 September) for 2006.

Each region exhibited a prominent bright-band signature (enhanced reflectivity) in the stratiform profiles (Figure 9)

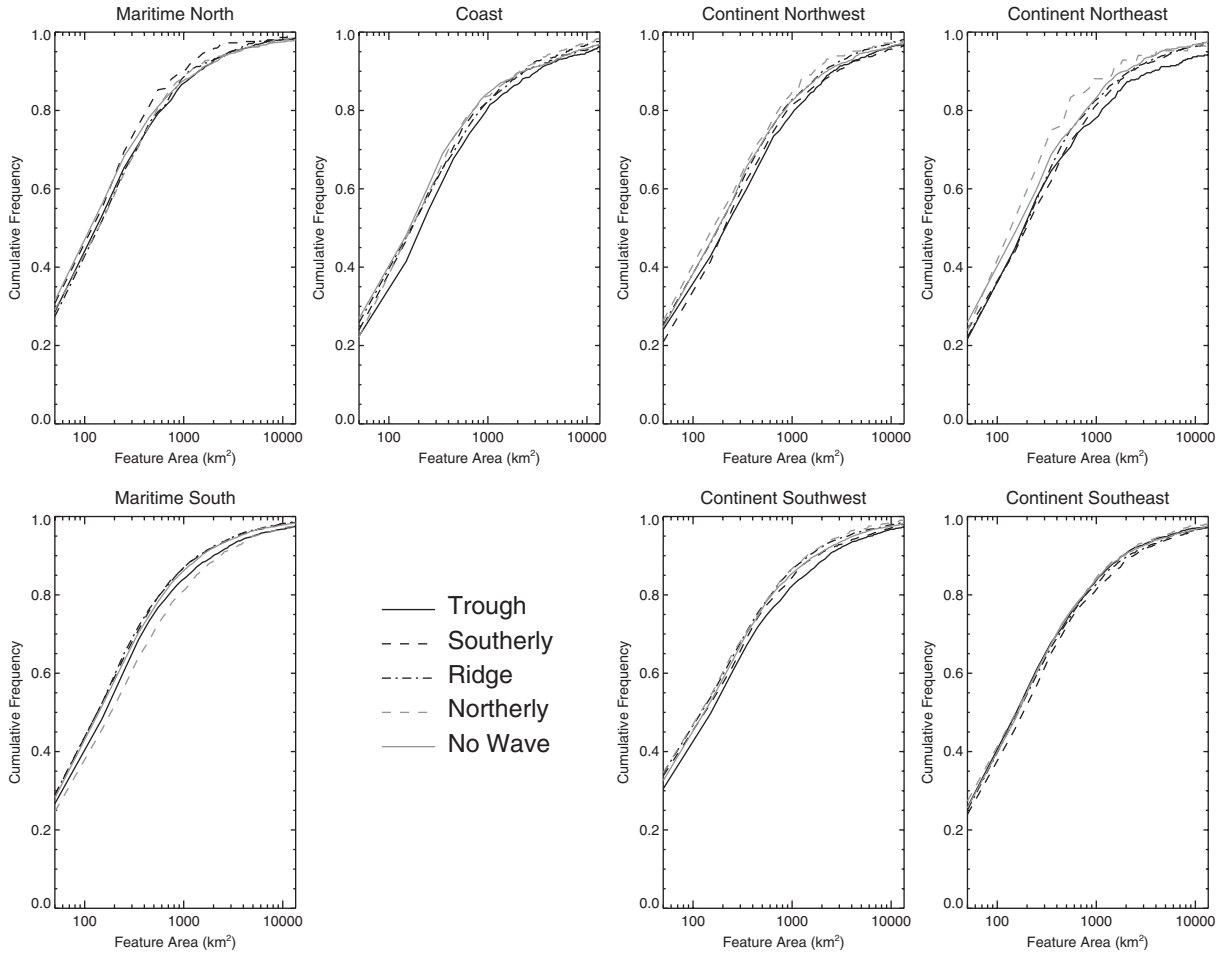

Figure 6. As in Figure 4, except for precipitation feature area.

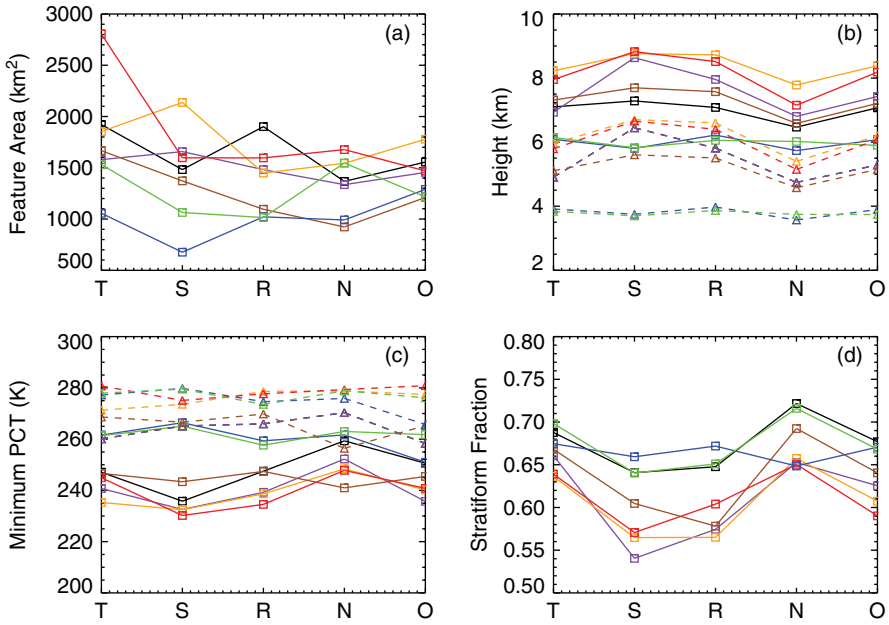

Figure 7. Mean values of (a) feature area, (b) maximum storm height (solid lines with open squares) and 30 dBZ height (dashed lines with open triangles), (c) 37 GHz (dashed lines with open triangles) and 85 GHz (solid lines with open squares) minimum PCTs, and (d) stratiform fraction during trough ('T'), southerly ('S'), ridge ('R'), and northerly ('N') AEW phase and when no AEW phase is identified ('O'). Continental northeast (red), continental northwest (orange), continental southeast (purple), continental southwest (brown), coastal (black), maritime north (green), and maritime south (blue) regions are displayed.

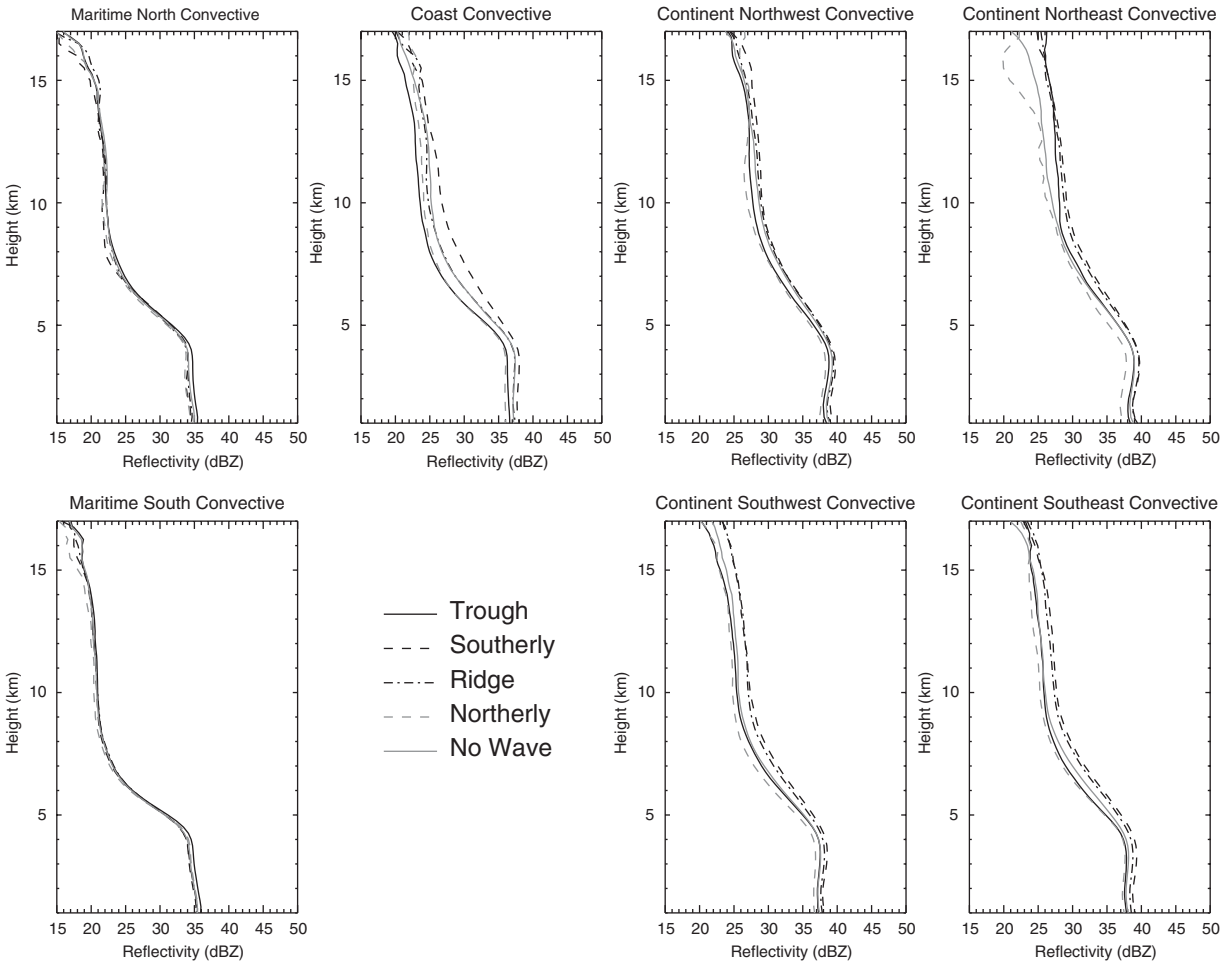

Figure 8. Mean convective vertical reflectivity profiles of TRMM precipitation radar observations for each study region. Trough (solid black), southerly (dashed black), ridge (dotted black), and northerly (dashed grey) AEW phase along with no identified AEW (solid grey) are shown.

near 4.5 km, well-established as the tropical melting level, with rapid decrease in reflectivity above. The bright band is primarily due to aggregates of ice particles descending through the 0°C isotherm, which begin to melt resulting in a stronger radar reflectivity due to differences in the dielectric constant between ice and water. Continental locations displayed more variability between AEW regimes above the bright band, while maritime regions showed almost no differences.

A comparison of regional vertical reflectivity profiles (Figure 10) closely resembled results from Fuentes *et al.* (2008), where convective profiles (Figure 10(a)) were more intense over land and in the coastal region than over the ocean. More intense convective components were confirmed by two separate proxies for convective intensity, listed in Table III. First, mean maximum 30 dBZ heights (DeMott and Rutledge, 1998) varied zonally, with continental north ($\sim$ 6.1 km) and south ($\sim$ 5.3 km) regions displaying the greatest 30 dBZ heights, decreasing westward in the coastal (4.7 km) and maritime (3.8 km) regions. Continental convection has been shown to contain stronger updraughts (e.g. Zipser and LeMone, 1980; Lucas *et al.*, 1994) allowing greater hydrometeor lofting, resulting in increased ice and graupel (i.e. mixed-phase) production aloft. The presence of ice hydrometeors aloft results in decreased mean minimum 85 GHz PCT values (Heymsfield and Fulton, 1988; Mohr and Zipser, 1996), or increased ice scattering signature, inland (shown later).

Near the surface, maritime convective reflectivity profiles continued to increase toward low levels, suggesting droplet growth mechanisms via warm rain (coalescence) processes. Continental and coastal regions were often associated with decreasing reflectivity towards the surface, indicating drop evaporation or drop breakup. Northern and southern domains exhibited similar convective reflectivity profiles below 6 km, with more variability aloft. Mean MSHs and 85 GHz PCTs (Table III) were nearly identical, suggesting that vertical growth and ice water path were also similar in a mean sense (discussed below).

Bright-band signatures in stratiform profiles (Figure 10(b)) were similar in magnitude in all regions except MarS, which was up to 2 dB weaker. Strong evaporative processes were observed in the ConNE region and to a lesser degree ConSE, inferred from the decrease of reflectivity below the bright band to low levels. The linear organization of continental MCSs would often lead to the presence of a rear inflow jet which may aid in the evaporative process. Oceanic and coastal regions continued to increase toward the surface, an indication of moist lower levels. Unlike convective profiles, which exhibited distinct separations for each region, stratiform profiles were tightly grouped, except the MarS profile which displayed lower reflectivity values below 5 km. Maritime reflectivity profiles decreased more rapidly above the bright band than in the coastal and continental regions, resulting in two distinct groupings from 5 km and upwards: maritime and continental. These differences in

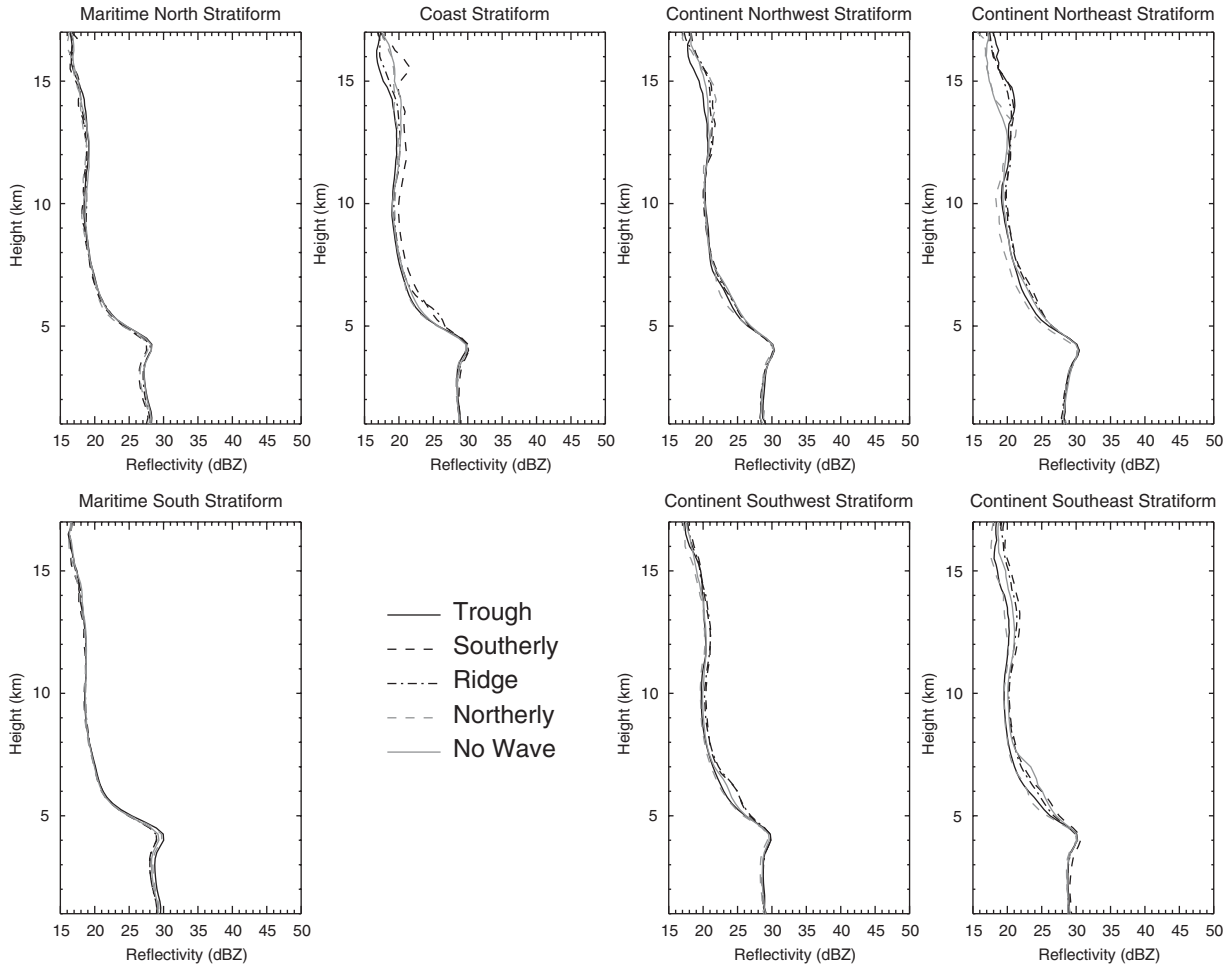

Figure 9. Same as Figure 8, except for stratiform component.

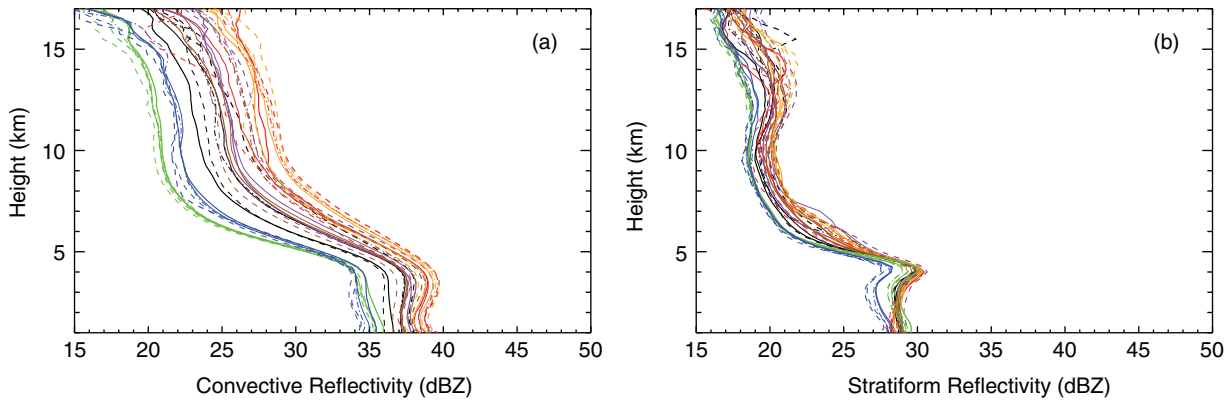

Figure 10. Mean (a) convective and (b) stratiform vertical reflectivity profiles for continental northeast (red), continental northwest (orange), continental southeast (purple), continental southwest (brown), coastal (black), maritime north (green), and maritime south (blue) regions. Line styles as in Figures 8–9, designating AEW phase.

reflectivity profiles suggested varying ice and liquid water vertical distributions in each region and by AEW regime.

The non-parametric Spearman's rho correlation coefficient (which is less sensitive to outlier data than Pearson's rho) was calculated using the convective profiles as the independent variable and the stratiform profiles as the dependent variable. Results showed significant high positive correlations for all regions (0.53–0.93; only MarN exhibiting values less than 0.63), indicating that stratiform profile strength increased with convective profile strength. Comparing these results by AEW regime to the characteristics expressed at the end of section 3.1 suggested that when stronger convective regions were present, the stratiform vertical reflectivity profiles exhibited stronger characteristics, possibly due to larger ice mass fluxes from the intense convective regions. Additionally, organized systems tend to establish broader mesoscale ascent due to the increased stratiform portion. In leading-convective, trailing-stratiform type systems (as found frequently over the continent), ascending front-to-rear flow from convective cells to the stratiform region transports convective ice particles into the upper stratiform regions. Growth via vapour deposition

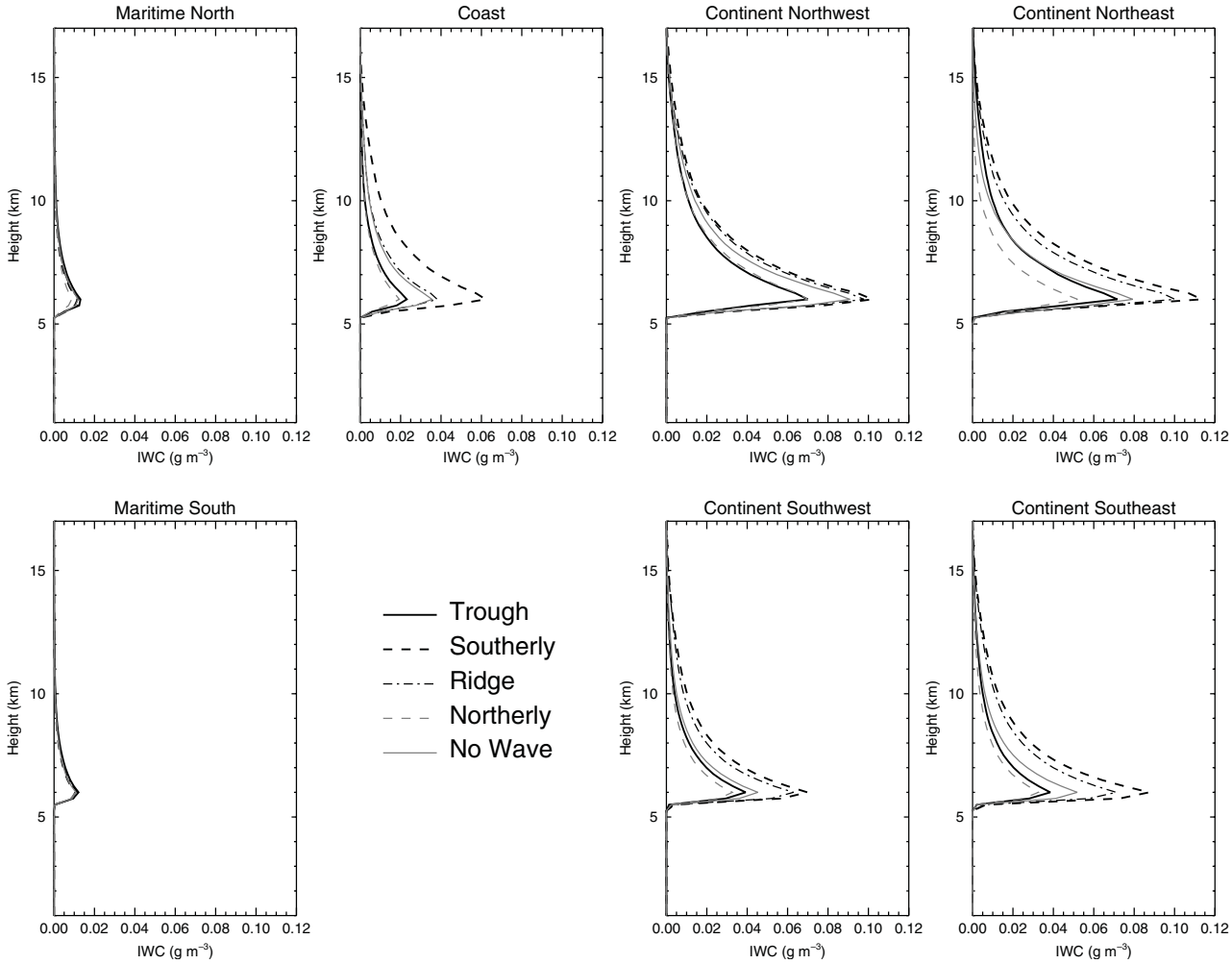

Figure 11. Same as Figure 8, except for ice water content.

during transport (Rutledge and Houze, 1987), along with aggregation during particle descent in the stratiform region results in larger particles. These processes result in larger particles throughout much of the vertical extent of the convective systems, which yields stronger stratiform reflectivity profiles.

Mean vertical profiles of IWC and LWC were calculated using both convective and stratiform points. Large differences in the vertical distributions of IWC (Figure 11) were revealed between regions. The continental regions contained the most ice water, with the coastal region containing less. Maritime regions contained the smallest ice mass contents. This suggested stronger updraughts inland, allowing ice microphysics to play a more important role in precipitation production at those locations. Contributions to total ice mass were found to be largely from the convective portion of storms (67–95%). As expected (due to the use of an M–Z relationship) this followed the distribution of the vertical profiles of convective reflectivity. The fact that the AEW southerly and ridge regimes contained larger amounts of ice water than other AEW regimes over land suggested the presence of significant updraughts, capable of producing large graupel, and probably even hail, particles that possess large fall speeds. This is consistent with lower stratiform fractions observed in these regions.

As suggested above, northern and southern region profiles were similar, though northern continental regions contained greater ice water throughout the profile than the southern regions. Mean minimum 37 GHz PCT was lower in ConSW than other continental regions (Table III), which might indicate that ice hydrometeors aloft were larger in the ConSW region as the 37 GHz channel is more sensitive to larger ice particles.

Over MarS, a larger mean 37 GHz PCT depression was observed compared to MarN. The explanation of large ice particles seems unlikely, given the similarities in both reflectivity and IWC profiles. Another possible explanation may be present in the vertical distributions of LWC (Figure 12). You *et al.* (2011) suggested that in the presence of large amounts of ice and liquid hydrometeors and surface rainfall (required for LWC to be calculated), the 37 GHz channel shows a stronger response than other microwave channels. More liquid water in MarS low-levels than MarN, along with similar IWC distributions, would support the larger 37 GHz depression in MarS. An increase in LWC was observed moving eastward; however, the relative profile shapes were quite different, with liquid water increasing to near-surface at each location except for the northern continental regions (where sub-cloud evaporation dominated). The contribution of the convective portion of systems to total liquid water mass was 40–68%, showing that stratiform contribution to liquid water mass was greater than for ice mass for all regions. Again variability was observed between AEW phases, with the southerly phase

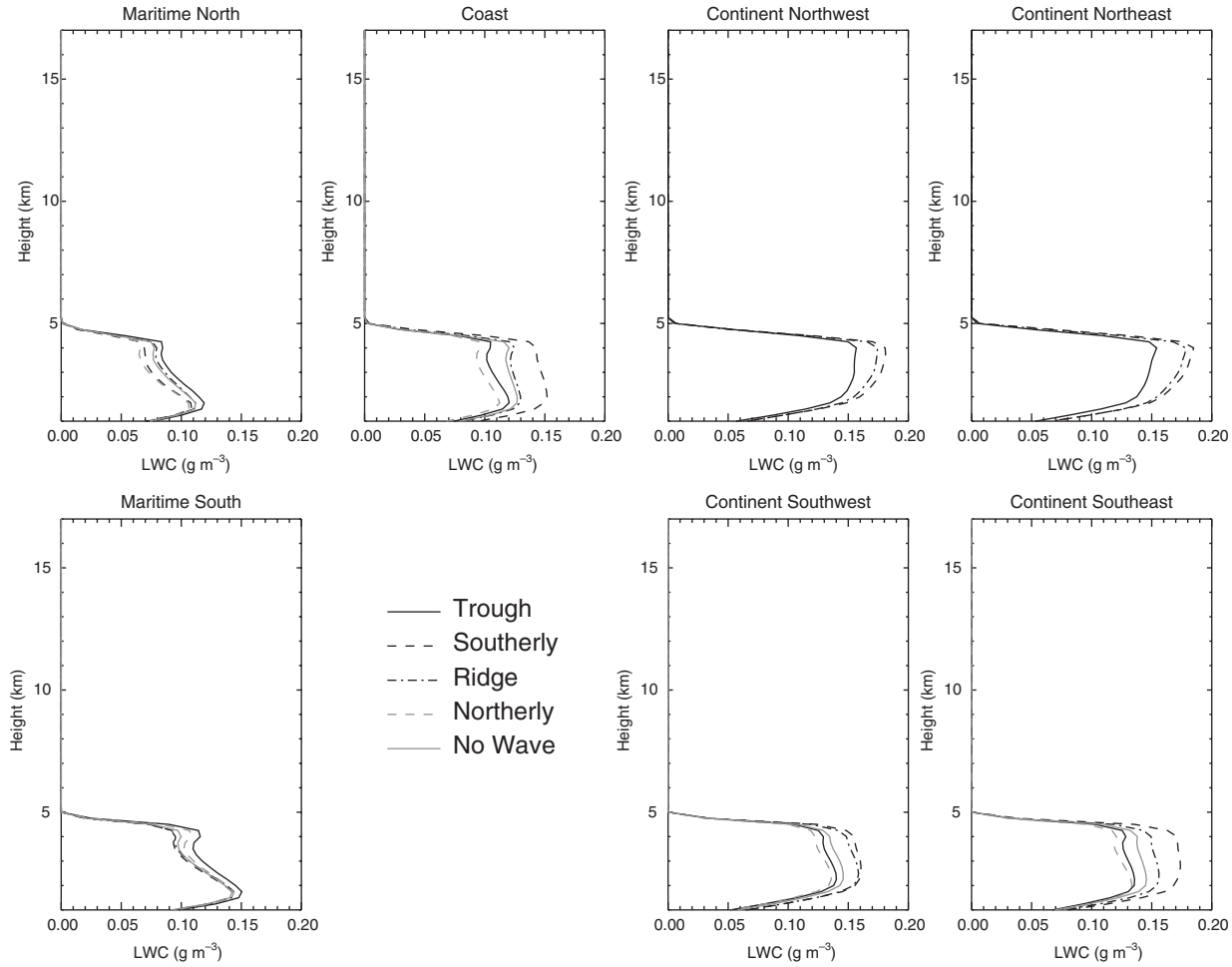

Figure 12. Same as Figure 8, except for liquid water content.

producing the largest amounts of liquid water in coastal and continental regions. Despite indications of more strong, isolated convective events (Figure 7), the southerly AEW phase produces larger ice and water mass than the other AEW regimes.

3.3. *Microphysical characteristics*

Due to the variability of horizontal and vertical characteristics it was of interest to try to explore microphysical characteristics in a limited way, based upon radar reflectivity. The previous section suggested how microphysical processes in the regions varied as a function of AEW regime. These processes contribute to determining the characteristics associated with the population of PFs in each region. Minimum 85 GHz PCT distributions (Figure 13) indicated a higher frequency of larger 85 GHz depressions (lower 85 GHz PCTs) over the continent, decreasing in occurrence westward into the Atlantic. Greater variability between AEW regimes was observed in the coastal and continental regions, but supported regional distributions of MSH (Figure 4), where taller storms corresponded to greater ice scattering signatures, and more intense convective systems by other metrics (i.e. 30 dBZ heights and vertical reflectivity profiles). While the same zonal trend was observed in the southern regions, all southern regions exhibited a smaller frequency of larger 85 GHz depressions than northern counterpart regions. Minimum 37 GHz PCT distributions (not shown) resulted in the same conclusions, albeit with less variability between AEW phases, suggesting a robust relationship between the convective metrics used in this study in each region.

Low values of 85 GHz PCT are indicative of a large IWP (e.g. Xu *et al.*, 2010), while low values of 37 GHz PCT are indicative of large ice particles or large amounts of mixed-phase particles. Therefore to determine both liquid and ice water contributions, IWP (Figure 14) and LWP (Figure 15) fractions (IWP or LWP divided by the sum of IWP and LWP, respectively) were calculated for every PF in each region as a function of AEW regime. All non-raining pixels were disregarded in the calculation of IWC and LWC. Following separation into convective and stratiform components, IWP and LWP fractions allow a basic interpretation of precipitation processes. High IWP fractions along with low LWP fractions suggest a strong dependence on ice-based microphysics. On the other hand, low IWP and high LWP fractions suggest strong warm-rain processes.

The difference in stratiform and convective frequency distributions is evident in each region. Higher (lower) frequencies of high IWP (LWP) fractions were observed in convective portions, with the reverse true for the stratiform portion. Despite these similarities, large variability was observed both between regions and across AEW regimes for IWP and LWP fractions (Figures 14–15). Maritime regions exhibited characteristics suggestive of warm-rain processes. The increased contribution of ice microphysics

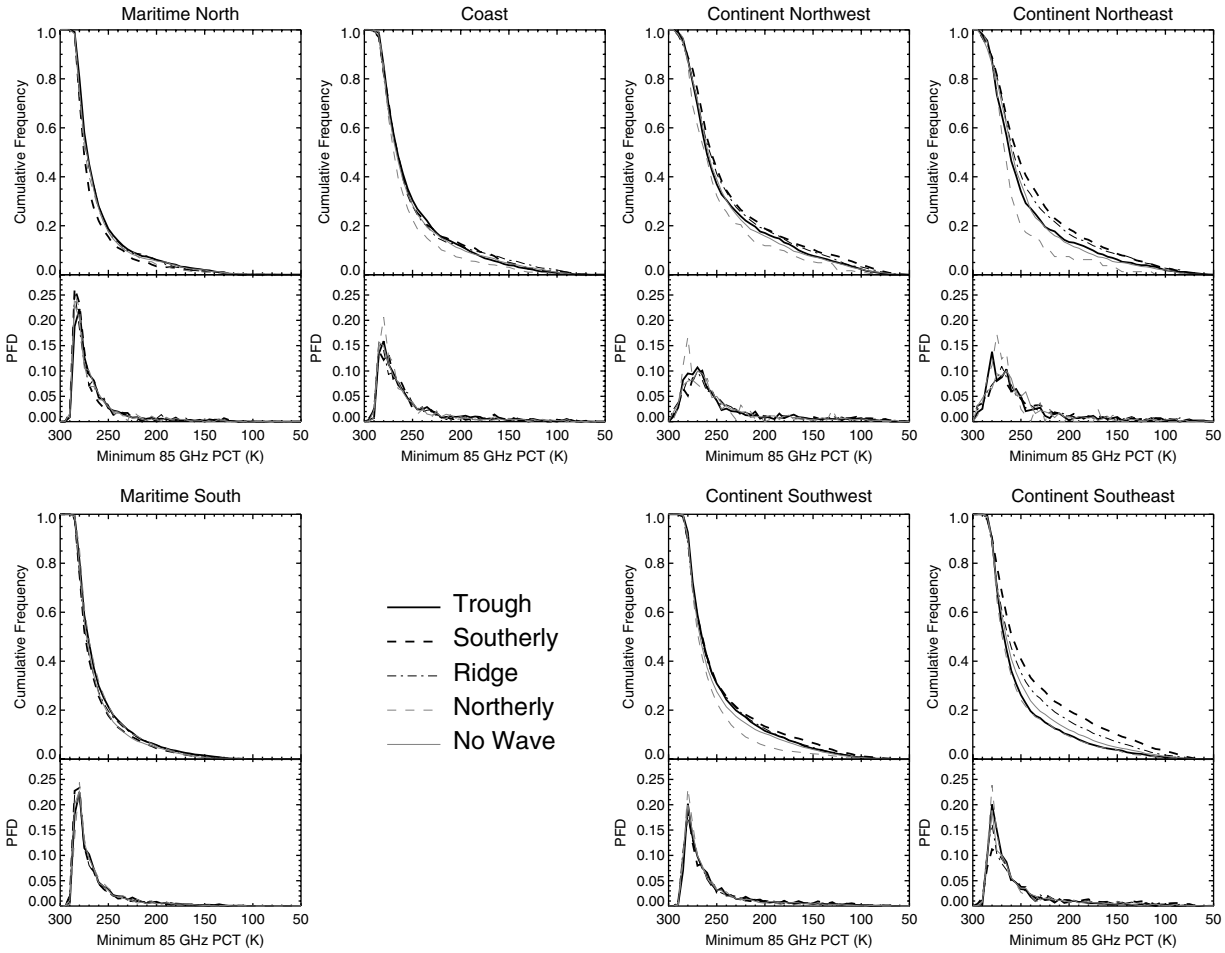

Figure 13. Cumulative (top) and probability (bottom) frequency distributions, for each study region, of minimum 85 GHz polarization corrected temperature. Line styles as in Figure 8.

is apparent moving inland. Southern continental regions exhibited a more apparent warm-rain signature, whereas the northern continental regions exhibited a signature more dependent upon ice-based microphysics.

Tighter grouping of AEW phase distributions was observed over oceanic regions, suggesting that system structure displayed greater homogeneity than observed inland. Convective distributions showed looser groupings across AEW phases than stratiform distributions in every continental (and coastal) region. This suggests that greater variability in convective microphysical structure was present. As mentioned previously, convective contributions dominated IWC, and to a lesser extent LWC, profiles. Additionally, steeper slopes in the oceanic and coastal distributions indicate a narrower range of ice and water mass fractions in these regions, whereas over the continent a greater spectrum of ice and water fractions was possible.

The southerly and ridge AEW phase systems produced more frequent higher IWP fractions in continental regions. This suggests that stronger updraughts existed during this phase, confirmed by higher MSH and 30 dBZ heights. Stratiform fractions shown in Figure 5 indicate a lower occurrence of large stratiform fraction in the continental regions during the southerly and ridge AEW regimes, while the trough phase displayed opposite characteristics: lower IWP fraction, higher LWP fraction, and higher occurrence of larger stratiform fractions. Fundamental differences in convective system morphology and microphysical processes seem to exist between regions and AEW regime.

4. Conclusion

A comparison of convective characteristics in seven distinct mesoscale regions influenced by the WAM was presented. Continental, coastal and maritime regions were defined based upon ground-radar observations during the 2006 AMMA field experiment examined in Guy *et al.* (2011), along with an additional continental region between the coastal and continental regions mentioned to provide semi-continuous zonal coverage. Adjacent continental and maritime regions were included to the south to allow investigation of meridional variability. A 13-year 'climatology' using precipitation features based upon contiguous TRMM satellite PR pixels was developed using PR and TMI (37 and 85 GHz) observations. These data were subset by AEW phase (trough, southerly, ridge and northerly) and when no AEW phase was identified, using ERA-Interim winds and applying the Berry *et al.* (2007) AEW trough tracking algorithm, with additional phase identification.

Frequency distributions showed that PF populations in southern regions far outnumbered their northern counterparts. Southern regions experience a seasonal cycle of PFs more varied than the northern regions. For example, Fink *et al.* (2006) in a study of a subset of the ConSE region

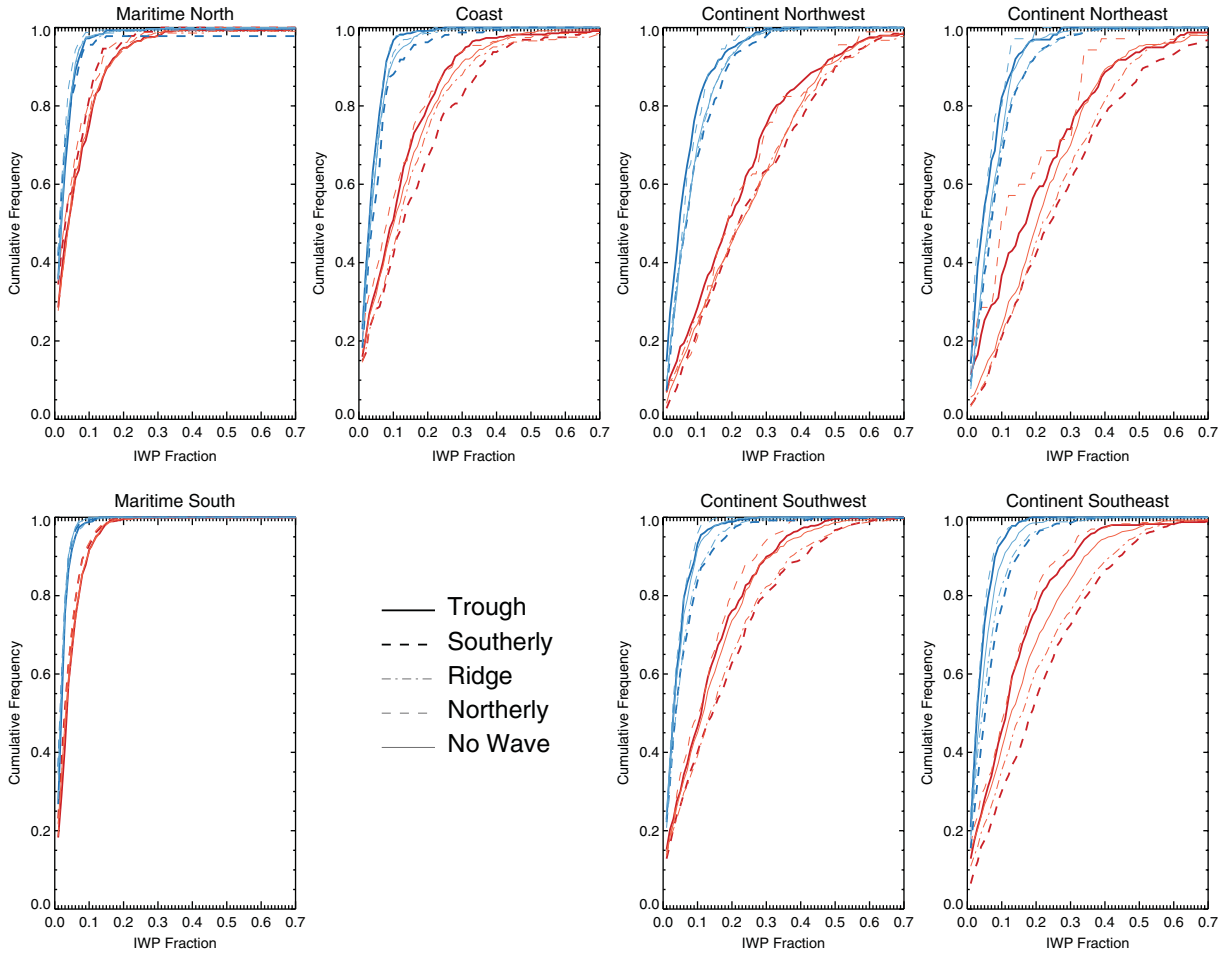

Figure 14. As in Figure 4, except for ice water path fraction, defined as ice water path divided by the sum of ice and liquid water path. Distributions are additionally separated by convective (red) and stratiform (blue) classification.

revealed that Sahelian-type squall line MCSs (SLMCSs) were common outside the peak WAM season, while organized MCS convection exhibited different precipitation characteristics (Sudano-Guinean; slower-moving, shorter-lived, and smaller areal coverage) during the monsoon season. Vertical extent and associated characteristics (e.g. 85 GHz depressions) may also be affected by this cycle. Northern regions primarily experienced fast-moving SLMCSs throughout the study, which may help to explain some latitudinal variability between regions. Feature association with AEW regime was in general agreement with previous studies, despite the fact that those studies focused largely on the generation and lysis of MCSs with respect to AEWs. Preferential occurrence east of AEW troughs near the continental sites and west of and in the trough near the coast and Atlantic was observed. All regions, except continental north, had a substantial number of PFs not associated with an AEW regime.

Magnitudes of regional differences were larger than AEW regime variability for convective characteristics, in agreement with the findings of Guy *et al.* (2011). Mean storm top and maximum 30 dBZ heights were lowest over maritime regions and increased moving eastward. The occurrence of tall (> 10 km) storm top heights also increased over land. Though feature area increased from ocean to land, stratiform fraction trended slightly opposite, decreasing from the Atlantic over land. Schumacher and Houze (2003, 2006) observed a similar trend in stratiform fraction, though the differences between ocean and continent were larger than observed in this study. Enhanced mean 85 GHz depressions were observed over land, in agreement with previous studies.

Mean values during AEW phases and when no AEW was present indicated variability of convective characteristics as a function of synoptic regime. Characteristics as a function of easterly phase differed from those found by Petersen and Boccippio (2004). The trough phase displayed a widespread convective signature, while the southerly phase generally indicated more isolated, intense convection. Convective characteristics during the ridge phase were slightly more intense than during the trough phase. A decrease in convective strength was observed during the northerly AEW phase. Convection occurring when no AEW was identified was similar to that in the southerly AEW regimes, with an increased stratiform signature.

The separation of convective reflectivity profiles by region was evident, while stratiform reflectivity profiles displayed similar features. The most notable differences appeared near the surface, likely due to environmental characteristics (moist over ocean and coast, drier inland; especially in northern regions). Influence of AEW regimes was more apparent in frequency distributions and vertical reflectivity profiles in the coastal and continental regions than the maritime regions. Generally, the southerly, and to a lesser degree the ridge regime, resulted in strengthened convective intensity metrics over land, revealing enhancement of the convective portion of MCSs. Of interest, the distribution of stratiform fraction showed large variability between AEW

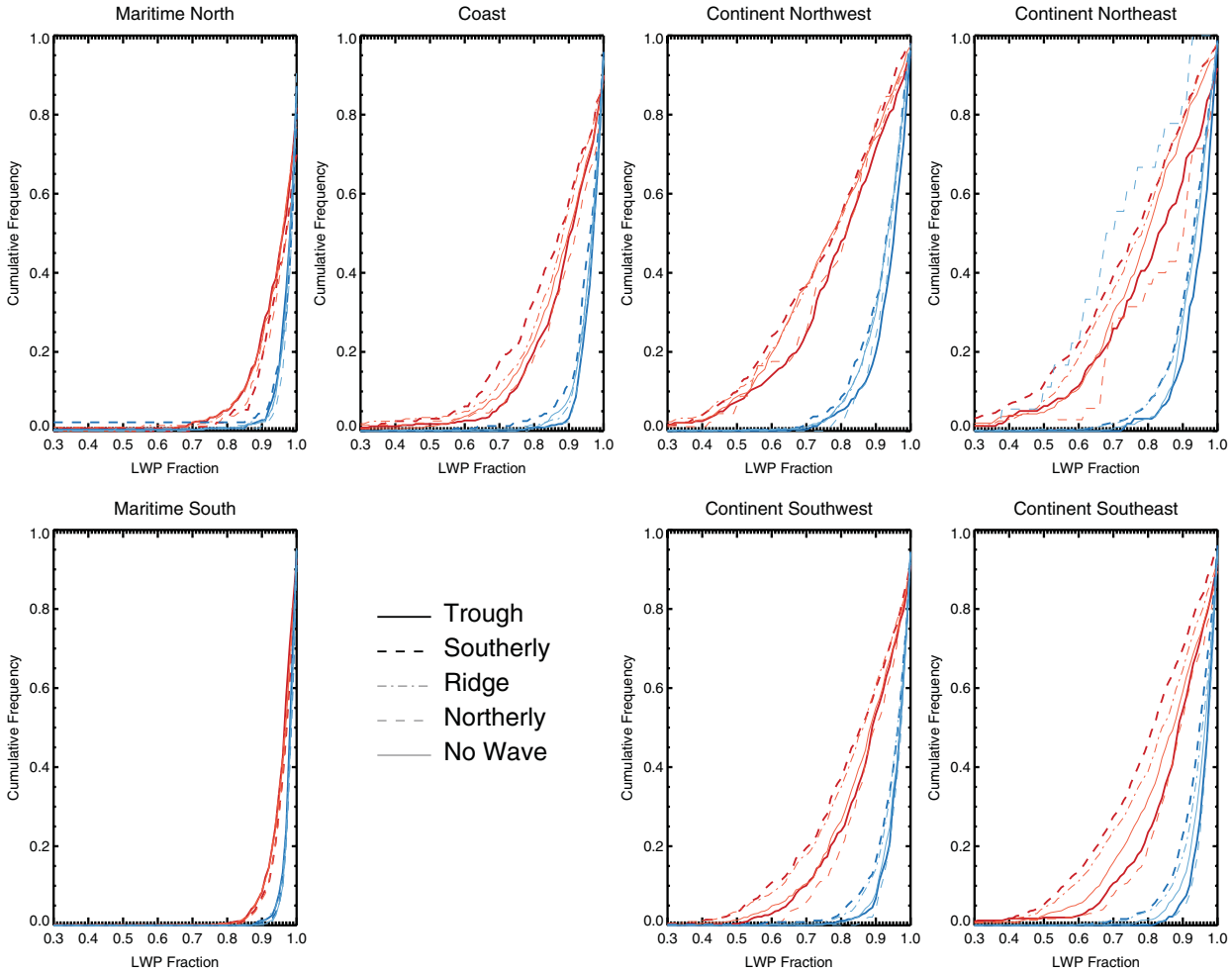

Figure 15. As in Figure 14, except for liquid water path fraction, defined as liquid water path divided by the sum of ice and liquid water path.

regimes despite less variability in area distributions between AEW regimes. This result is important given the implications of differences of latent heating interaction with the larger environment. Characteristics of PFs that occurred during the no-wave regime displayed convective characteristics similar to those during AEW regimes, suggesting that while AEWs can act to enhance certain features of convective systems, regional variability of thermodynamic environments play a crucial role in system organization.

Microphysical characteristics displayed large variability both regionally and between AEW regimes. Vertical profiles of IWC revealed values up to an order of magnitude greater over the continent compared to maritime regions, with peak values differing by a factor of three between AEW regimes. Profiles of LWC also indicated variability between AEW regimes, though less difference in regional LWC profiles was observed. The convective portion of systems dominated contribution to IWC and contributed approximately half of LWC, where the stratiform portion provided a much larger contribution. Analysis of IWP and LWP fractions suggested that ice precipitation processes played a greater role in northern regions than adjacent southern regions over land. Indications of warm-rain processes were stronger in the maritime and southwest continental regions.

As this study uses 'snapshots' of convective events via TRMM satellite overpasses, detailed information regarding life-cycle phasing with AEW regime cannot be implied reliably through these data. Unique kinematic and microphysical structures exist as a function of the life cycle of MCSs. Because many MCSs moved faster than AEWs, and therefore interaction with more than one phase of an AEW was possible, aliasing of life-cycle characteristics was also possible. Despite this constraint, many useful details have been learned regarding the difference in characteristics of convection as a function of AEW phase and when no wave is present.

The extent of the free tropospheric moisture conditions have been suggested to play an important role in the variability of convection at synoptic scales (e.g. Roca *et al.*, 2005; Lafore *et al.*, 2011). Future work characterizing the changes in thermodynamic and dynamic environmental structure on a regional scale similar to this study could help to illuminate scale interactions before, when, and after convection is present.

Analysis of the variability involved in the zonal and meridional convective and microphysical characteristics may help to improve West African model simulations and precipitation retrieval algorithms, especially over continental Africa where observations are sparse. Combined observations and simulations of convective systems in the different regions studied here would help the understanding of microphysical processes involved in precipitation production and convective maintenance in each region. Analysis of the melting layer, where both ice and liquid water exist, is important in understanding convective

system mass distribution. This information could help our understanding of feedback mechanisms between spatial scales and intra-storm, allowing greater understanding of WAM processes.

Acknowledgements

This research was supported by the NASA CEAS fellowship grant NNX08AT77G and the NASA Precipitation Measurement Mission under grant NNX10AG88G. The authors would like to acknowledge Chuntao Liu for providing information and software for the interpretation and analysis of the University of Utah TRMM Precipitation Feature database. We would also like to thank the reviewers for suggestions that improved the manuscript.

References

Aspliden CI, Tourre Y, Sabine JB. 1976. Some climatological aspects of West African disturbance lines during GATE. *Mon. Weather Rev.* **104**: 1029–1035.

Bain CL, Parker DJ, Dixon N, Fink AH, Taylor CM, Brooks B, Milton SF. 2011. Anatomy of an observed African easterly wave in July 2006. *Q. J. R. Meteorol. Soc.* **137**: 923–933.

Barnes GM, Sieckman K. 1984. The environment of fast- and slow-moving tropical mesoscale convective cloud lines. *Mon. Weather Rev.* **112**: 1782–1794.

Barthe C, Asencio N, Lafore J-P, Chong M, Campistron B, Cazenave F. 2010. Multi-scale analysis of the 2527 July 2006 convective period over Niamey: Comparison between Doppler radar observations and simulations. *Q. J. R. Meteorol. Soc.* **136**(S1): 190–208.

Berry GJ. 2009. '*African easterly waves and convection*.' PhD dissertation, 209 pp. Department of Atmospheric and Environmental Sciences, University at Albany, State University of New York.

Berry GJ, Thorncroft CD. 2005. Case study of an intense African easterly wave. *Mon. Weather Rev.* **133**: 752–766.

Berry GJ, Thorncroft CD, Hewson T. 2007. African easterly waves during 2004 Analysis using objective techniques. *Mon. Weather Rev.* **135**: 1251–1267.

Bolton D. 1984. Generation and propagation of African squall lines. *Q. J. R. Meteorol. Soc.* **110**: 695–721.

Bouniol D, Delanoë J, Duroure C, Protat A, Giraud V, Penide G. 2010. Microphysical characterisation of West African MCS anvils. *Q. J. R. Meteorol. Soc.* **136**(S1): 323–344.

Burpee RW. 1974. Characteristics of North African easterly waves during the summers of 1968 and 1969. *J. Atmos. Sci.* **31**: 1556–1570.

Carey LD, Rutledge SA. 2000. The relationship between precipitation and lightning in tropical island convection: A C-band polarimetric radar study. *Mon. Weather Rev.* **128**: 2687–2710.

Carlson TN. 1969. Some remarks on African disturbances and their progress over the tropical Atlantic. *Mon. Weather Rev.* **97**: 716–726.

Cetrone J, Houze Jr RA. 2009. Anvil clouds of tropical mesoscale convective systems in monsoon regions. *Q. J. R. Meteorol. Soc.* **135**: 305–317.

Cetrone J, Houze Jr RA. 2011. Leading and trailing anvil clouds of West African squall lines. *J. Atmos. Sci.* **68**: 1114–1123.

Cifelli R, Nesbitt SW, Rutledge SA, Petersen WA, Yuter S. 2007. Radar characteristics of precipitation features in the EPIC and TEPPS regions of the east Pacific. *Mon. Weather Rev.* **135**: 1576–1595.

D'Amato N, Lebel T. 1998. On the characteristics of the rainfall events in the Sahel with a view to the analysis of climatic variability. *Int. J. Climatol.* **18**: 955–974.

DeLonge MS, Fuentes JD, Chan S, Kucera PA, Joseph E, Gaye AT, Daouda B. 2010. Attributes of mesoscale convective systems at the landocean transition in Senegal during NASA African Monsoon Multidisciplinary Analyses 2006. *J. Geophys. Res.* **115**: D10213, DOI: 10.1029/2009JD012518.

DeMott CA, Rutledge SA. 1998. The vertical structure of TOGA COARE convection. Part I: Radar echo distributions. *J. Atmos. Sci.* **55**: 2730–2747.

Diedhiou A, Janicot S, Viltard A, de Felice P, Laurent H. 1999. Easterly wave regimes and associated convection over West Africa and tropical Atlantic: Results from the NCEP/NCAR and ECMWF reanalyses. *Clim. Dyn.* **15**: 795–822.

Duvel JP. 1990. Convection over tropical Africa and the Atlantic Ocean during northern summer. Part II: Modulation by easterly waves. *Mon. Weather Rev.* **118**: 1855–1868.

Eldridge RH. 1957. A synoptic study of West African disturbance lines. *Q. J. R. Meteorol. Soc.* **83**: 303–314.

Evaristo R, Scialom G, Viltard N, Lemaître Y. 2010. Polarimetric signatures and hydrometeor classification of West African squall lines. *Q. J. R. Meteorol. Soc.* **136**(S1): 272–288.

Fink AH, Reiner A. 2003. Spatiotemporal variability of the relation between African easterly waves and West African squall lines in 1998 and 1999. *J. Geophys. Res.* **108**: 4332, DOI: 10.1029/2002JD002816.

Fink AH, Vincent DG, Ermert V. 2006. Rainfall types in the West African Sudanian zone during the summer monsoon 2002. *Mon. Weather Rev.* **134**: 2143–2164.

Fortune M. 1980. Properties of African squall lines inferred from time-lapse satellite imagery. *Mon. Weather Rev.* **108**: 153–168.

Frank WM. 1978. The life cycles of GATE convective systems. *J. Atmos. Sci.* **35**: 1256–1264.

Fuentes JD, Geerts B, Dejene T, D'Odorico P, Joseph E. 2008. Vertical attributes of precipitation systems in West Africa and adjacent Atlantic Ocean. *Theor. Appl. Climatol.* **92**: 181–193.

Geerts B, Dejene T. 2005. Regional and diurnal variability of the vertical structure of precipitation systems in Africa based on spaceborne radar data. *J. Climate* **18**: 893–916.

Gu GJ, Adler RF, Huffman GJ, Curtis S. 2004. African easterly waves and their association with precipitation. *J. Geophys. Res.* **109**: D04101, DOI: 10.1029/2003JD003967.

Guy N, Rutledge SA, Cifelli R. 2011. Radar characteristics of continental, coastal and maritime convection observed during AMMA/NAMMA. *Q. J. R. Meteorol. Soc.* **137**: 1241–1256.

Hamilton RA, Archbold JW, Douglas CKM. 1945. Meteorology of Nigeria and adjacent territory. *Q. J. R. Meteorol. Soc.* **71**: 231–264.

Heymsfield GM, Fulton R. 1988. Comparison of high-altitude remote aircraft measurements with the radar structure of an Oklahoma thunderstorm: Implications for precipitation estimation from space. *Mon. Weather Rev.* **116**: 1157–1174.

Hodges KI, Thorncroft CD. 1997. Distribution and statistics of African mesoscale convective weather systems based on the ISCCP Meteosat imagery. *Mon. Weather Rev.* **125**: 2821–2837.

Houze Jr RA. 1977. Structure and dynamics of a tropical squall-line system. *Mon. Weather Rev.* **105**: 1540–1567.

Houze Jr RA, Betts AK. 1981. Convection in GATE. *Rev. Geophys.* **19**: 541–576.

Houze Jr RA, Biggerstaff MI, Rutledge SA, Smull BF. 1989. Interpretation of Doppler weather radar displays of midlatitude mesoscale convective systems. *Bull. Am. Meteorol. Soc.* **70**: 608–619.

Johnson RH, Aves SL, Ciesielski PE, Keenan TD. 2005. Organization of oceanic convection during the onset of the 1998 East Asian summer monsoon. *Mon. Weather Rev.* **133**: 131–148.

Kiladis GN, Thorncroft CD, Hall NMJ. 2006. Three-dimensional structure and dynamics of African easterly waves. Part I: Observations. *J. Atmos. Sci.* **63**: 2212–2230.

Kummerow C, Barnes W, Kozu T, Shiue J, Simpson J. 1998. The Tropical Rainfall Measuring Mission (TRMM) sensor package. *J. Atmos. Oceanic Technol.* **15**: 809–817.

Kummerow C, Simpson J, Thiele O, Barnes W, Chang ATC, Stocker E, Adler RF, Hou A, Kakar R, Wentz F, Ashcroft P, Kozu T, Hong Y, Okamoto K, Iguchi T, Kuroiwa H, Im E, Haddad Z, Huffman G, Ferrier B, Olson WS, Zipser E, Smith EA, Wilheit TT, North G, Krishnamurti T, Nakamura K. 2000. The status of the Tropical Rainfall Measuring Mission (TRMM) after two years in orbit. *J. Appl. Meteorol.* **39**: 1965–1982.

Lafore J-P, Flamant C, Guichard F, Parker DJ, Bouniol D, Fink AH, Giraud V, Gosset M, Hall N, Höller H, Jones SC, Protat A, Roca R, Roux F, Saïd F, Thorncroft CD. 2011. Progress in understanding of weather systems in West Africa. *Atmos. Sci. Lett.* **12**: 7–12.

Lafore J-P, Redelsperger J-L, Jaubert G. 1988. Comparison between a three-dimensional simulation and Doppler radar data of a tropical squall line: Transports of mass, momentum, heat, and moisture. *J. Atmos. Sci.* **45**: 3483–3500.

Laing AG, Carbone R, Levizzani V, Tuttle J. 2008. The propagation and diurnal cycles of deep convection in northern tropical Africa. *Q. J. R. Meteorol. Soc.* **134**: 93–109.

Laurent H, D'Amato N, Lebel T. 1998. How important is the contribution of the mesoscale convective complexes to the Sahelian rainfall? *Phys. Chem. Earth* **23**: 629–633.

Le Barbé L, Lebel T. 1997. Rainfall climatology of the HAPEX-Sahel region during the years 19501990. *J. Hydrol.* **188–189**: 43–73.

Leppert II KD, Petersen WA. 2010. Electrically active hot towers in African easterly waves prior to tropical cyclogenesis. *Mon. Weather Rev.* **138**: 663–687.

Liu CT, Zipser EJ, Cecil DJ, Nesbitt SW, Sherwood S. 2008. A cloud and precipitation feature database from nine years of TRMM observations. *J. Appl. Meteorol. Clim.* **47**: 2712–2728.
Lucas C, Zipser EJ, Lemone MA. 1994. Vertical velocity in oceanic convection off tropical Australia. *J. Atmos. Sci.* **51**: 3183–3193.
Machado LAT, Duvel J-P, Desbois M. 1993. Diurnal variations and modulation by easterly waves of the size distribution of convective cloud clusters over West Africa and the Atlantic Ocean. *Mon. Weather Rev.* **121**: 37–49.
Mathon V, Laurent H, Lebel T. 2002. Mesoscale convective system rainfall in the Sahel. *J. Appl. Meteorol.* **41**: 1081–1092.
Mekonnen A, Thorncroft CD, Aiyyer AR. 2006. Analysis of convection and its association with African easterly waves. *J. Climate* **19**: 5405–5421.
Mohr KI, Thorncroft CD. 2006. Intense convective systems in West Africa and their relationship to the African easterly jet. *Q. J. R. Meteorol. Soc.* **132**: 163–176.
Mohr KI, Zipser EJ. 1996. Mesoscale convective systems defined by their 85-GHz ice scattering signature: Size and intensity comparison over tropical oceans and continents. *Mon. Weather Rev.* **124**: 2417–2437.
Moncrieff MW. 1992. Organized convective systems: Archetypal dynamical models, mass and momentum flux theory, and parametrization. *Q. J. R. Meteorol. Soc.* **118**: 819–850.
Nesbitt SW, Zipser EJ. 2003. The diurnal cycle of rainfall and convective intensity according to three years of TRMM measurements. *J. Climate* **16**: 1456–1475.
Nesbitt SW, Zipser EJ, Cecil DJ. 2000. A census of precipitation features in the Tropics using TRMM: Radar, ice scattering, and lightning observations. *J. Climate* **13**: 4087–4106.
Nicholls SD, Mohr KI. 2010. An analysis of the environments of intense convective systems in West Africa in 2003. *Mon. Weather Rev.* **138**: 3721–3739.
Nitta T, Nakagomi Y, Suzuki Y, Hasegawa N, Kadokura A, 1985. Global analysis of the lower tropospheric disturbances in the Tropics during the northern summer of the FGGE year. I. Global features of the disturbances. *J. Meteorol. Soc. Jpn* **63**: 1–19.
Payne SW, McGarry MM. 1977. The relationship of satellite inferred convective activity to easterly waves over West Africa and the adjacent ocean during Phase III of GATE. *Mon. Weather Rev.* **105**: 413–420.
Penide G, Giraud V, Bouniol D, Dubuisson P, Duroure C, Protat A, Cautenet S. 2010. Numerical simulation of the 7 to 9 September 2006 AMMA mesoscale convective system: Evaluation of the dynamics and cloud microphysics using synthetic observations. *Q. J. R. Meteorol. Soc.* **136**(S1): 304–322.
Petersen WA, Boccippio DJ. 2004. 'Variability of convective structure and lightning activity in tropical easterly waves.' Paper 5B.1 in *Preprints, 26th Conference on Hurricanes and tropical meteorology, Miami Beach, Florida*. Am. Meteorol. Soc.
Petersen WA, Rutledge SA. 2001. Regional variability in tropical convection: Observations from TRMM. *J. Climate* **14**: 3566–3586.
Petersen WA, Cifelli R, Boccippio DJ, Rutledge SA, Fairall C. 2003. Convection and easterly wave structures observed in the eastern Pacific warm pool during EPIC-2001. *J. Atmos. Sci.* **60**: 1754–1773.
Petersen WA, Christian HJ, Rutledge SA. 2005. TRMM observations of the global relationship between ice water content and lightning. *Geophys. Res. Lett.* **32**: L14819, DOI: 10.1029/2005GL023236.
Protat A, Delanoë J, Plana-Fattori A, May PT, O'Connor EJ. 2010. The statistical properties of tropical ice clouds generated by the West African and Australian monsoons, from ground-based radar–lidar observations. *Q. J. R. Meteorol. Soc.* **136**(S1): 345–363.
Pytharoulis I, Thorncroft CD. 1999. The low-level structure of African easterly waves in 1995. *Mon. Weather Rev.* **127**: 2266–2280.
Redelsperger J-L, Diongue A, Diedhiou A, Ceron J-P, Diop M, Gueremy J-F, Lafore J-P. 2002. Multi-scale description of a Sahelian synoptic weather system representative of the West African monsoon. *Q. J. R. Meteorol. Soc.* **128**: 1229–1257.
Redelsperger J-L, Thorncroft CD, Diedhiou A, Lebel T, Parker DJ, Polcher J. 2006. African Monsoon Multidisciplinary Analysis: An international research project and field campaign. *Bull. Am. Meteorol. Soc.* **87**: 1739–1746.
Reed RJ, Norquist DC, Recker EE. 1977. The structure and properties of African wave disturbances as observed during Phase III of GATE. *Mon. Weather Rev.* **105**: 317–333.
Riemann-Campe K, Fraedrich K, Lunkeit F. 2009. Global climatology of convective available potential energy (CAPE) and convective inhibition (CIN) in ERA-40 reanalysis. *Atmos. Res.* **93**: 534–545.
Roca R, Lafore J-P, Piriou C, Redelsperger J-L. 2005. Extratropical dry-air intrusions into the West African monsoon midtroposphere: An important factor for the convective activity over the Sahel. *J. Atmos. Sci.* **62**: 390–407.
Rowell DP, Milford JR. 1993. On the generation of African squall lines. *J. Climate* **6**: 1181–1193.
Rutledge SA, Houze Jr RA. 1987. A diagnostic modelling study of the trailing stratiform region of a midlatitude squall line. *J. Atmos. Sci.* **44**: 2640–2656.
Sall SM, Sauvageot H. 2005. Cyclogenesis off the African coast: The case of *Cindy* in August 1999. *Mon. Weather Rev.* **133**: 2803–2813.
Schumacher C, Houze Jr RA. 2003. Stratiform rain in the Tropics as seen by the TRMM precipitation radar. *J. Climate* **16**: 1739–1756.
Schumacher C, Houze Jr RA. 2006. Stratiform precipitation production over sub-Saharan Africa and the tropical East Atlantic as observed by TRMM. *Q. J. R. Meteorol. Soc.* **132**: 2235–2255.
Simmons A, Uppala S, Dee D, Kobayashi S. 2007. '*ERA-Interim: New ECMWF reanalysis products from 1989 onwards.*' ECMWF Newsletter 110, 25–35.
Sommeria G, Testud J. 1984. COPT 81: A field experiment designed for the study of dynamics and electrical activity of deep convection in continental tropical regions. *Bull. Am. Meteorol. Soc.* **65**: 4–10.
Tao W-K, Lang S, Simpson J, Adler R. 1993. Retrieval algorithms for estimating the vertical profiles of latent heat release: Their applications for TRMM. *J. Meteorol. Soc. Jpn* **71**: 685–700.
Tao W-K, Lang S, Zeng XP, Shige S, Takayabu Y. 2010. Relating convective and stratiform rain to latent heating. *J. Climate* **23**: 1874–1893.
Thorncroft CD, Hodges K. 2001. African easterly wave variability and its relationship to Atlantic tropical cyclone activity. *J. Climate* **14**: 1166–1179.
Thorncroft CD, Hall NMJ, Kiladis GN. 2008. Three-dimensional structure and dynamics of African easterly waves. Part III: Genesis. *J. Atmos. Sci.* **65**: 3596–3607.
Tokay A, Short DA. 1996. Evidence from tropical raindrop spectra of the origin of rain from stratiform versus convective clouds. *J. Appl. Meteorol.* **35**: 355–371.
Tokay A, Kruger A, Krajewski WF, Kucera PA, Pereira Filho AJ. 2002. Measurements of drop size distribution in the southwestern Amazon basin. *J. Geophys. Res.* **107**: 8052, DOI: 10.1029/2001JD000355.
Toracinta ER, Cecil DJ, Zipser EJ, Nesbitt SW. 2002. Radar, passive microwave, and lightning characteristics of precipitating systems in the Tropics. *Mon. Weather Rev.* **130**: 802–824.
Xu WX, Zipser EJ, Liu CT. 2009. Rainfall characteristics and convective properties of Mei-Yu precipitation systems over south China, Taiwan, and the South China Sea. Part I: TRMM observations. *Mon. Weather Rev.* **137**: 4261–4275.
Xu WX, Zipser EJ, Liu CT, Jiang HY. 2010. On the relationships between lightning frequency and thundercloud parameters of regional precipitation systems. *J. Geophys. Res.* **115**: D12203, DOI: 10.1029/2009JD013385.
You YL, Liu GS, Wang Y, Cao J. 2011. On the sensitivity of Tropical Rainfall Measuring Mission (TRMM) Microwave Imager channels to overland rainfall. *J. Geophys. Res.* **116**: D12203, DOI: 10.1029/2010JD015345.
Zipser EJ. 1969. The role of organized unsaturated convective downdrafts in the structure and rapid decay of an equatorial disturbance. *J. Appl. Meteorol.* **8**: 799–814.
Zipser EJ, LeMone MA. 1980. Cumulonimbus vertical velocity events in GATE. Part II: Synthesis and model core structure. *J. Atmos. Sci.* **37**: 2458–2469.
Zipser EJ, Liu CT, Cecil DJ, Nesbitt SW, Yorty DP. 2006. Where are the most intense thunderstorms on Earth? *Bull. Am. Meteorol. Soc.* **87**: 1057–1071.

